Petrologic Reconstruction of the Tieshan Magma Plumbing System: Implications for the Genesis of Magmatic-Hydrothermal Ore Deposits within Originally Water-Poor Magmatic Systems

Jin-Sheng Zhou[1], Qiang Wang[1,2,3]*, Derek A. Wyman [4] and Zhen-Hua Zhao[5]

[1]State Key Laboratory of Isotope Geochemistry, Guangzhou Institute of Geochemistry, Chinese Academy of Sciences, Guangzhou 510640, China; [2]CAS Center for Excellence in Tibetan Plateau Earth Sciences, Beijing 100101, China; [3]College of Earth and Planetary Sciences, University of Chinese Academy of Sciences, Beijing 100049, China; [4]School of Geosciences, University of Sydney, NSW 2006, Australia; [5]Key laboratory of Mineralogy and Metallogeny, Guangzhou Institute of Geochemistry, Chinese Academy of Sciences, Guangzhou 510640, China

*Corresponding author. Telephone: + 86 20 85290277. Fax: +86 20 85290130. E-mail: wqiang@gig.ac.cn

ABSTRACT

Most genetic models for magmatic-hydrothermal ore deposits are based on the prerequisite that the parental magmas associated with mineralization are enriched in water ($> \sim 4$ wt %). However, it has been recognized that a number of magmatic-hydrothermal ore deposits also formed within tectono-magmatic settings that produce initially water-poor magmas such as Climax-type porphyry deposits. Here, we present a detailed reconstruction of the Tieshan magma plumbing system related to skarn-porphyry Cu–Fe–Au mineralization in the Edong district, in which primitive magmas typically show water-poor features. Applications of multiple thermodynamic calibrations on various magmatic units from the Tieshan and Tonglushan deposits provide a wealth of information regarding the structure and evolution of the transcrustal magmatic system. Petrographic observations and clinopyroxene-liquid thermobarometry calculations indicate that the Tieshan magmatic-hydrothermal system was fed by a deep crustal magma reservoir. An accurate picture of the evolution of H_2O within the magma plumbing system is presented using the plagioclase-liquid hygrometer in combination with the amphibole hygrometer. Three critical stages during the evolution of water within the plumbing system have been recognized, associated with H_2O contents of 0·8–1·7 wt %, 2·1–2·8 wt % and 3·2–4·6 wt %, respectively. The first enrichment of water in the magmas can be attributed to the separation and transfer of evolved melts from the deep magma reservoir to the shallow crust. Continuous cooling and solidification of the shallow magma body gave rise to the second enrichment of H_2O in residual melts, leading to magmas that were fertile for the formation of ore deposits. The detailed chemical evolution of the magma plumbing system was investigated using mineral trace element compositions in combination with the partition coefficients predicted by the lattice strain model. The earliest equilibrium melts are characterized by high Sr contents (the average $= 658 \pm 64$ ppm), suggesting that high Sr/Y signatures were likely derived from their magma sources or fractionation at deeper levels in initially water-poor environments. Variations of some particular geochemical fingerprints in equilibrium melts such as, Dy/Dy* and Eu/Eu*, also provide fundamental information on the evolution of the magma plumbing system. Our study confirms the critical role of a deep crustal magma reservoir on the formation of

magmatic-hydrothermal ore deposits. The fertility of magmas with respect to ore deposit formation was enhanced by the extraction and transfer of evolved magmas from the deep reservoir to shallower levels, particularly due to the enrichment of magmatic water contents. In addition, the presence of a deep magma reservoir also sustains the incremental growth of shallow magma chambers, which provide ore-forming fluids.

Key words: geothermobarometry; magma reservoir; magmatic volatiles; magmatic-hydrothermal ore deposit; trace element

INTRODUCTION

Magmatic-hydrothermal ore deposits, including porphyry, skarn and epithermal types, are the primary source for some of our society's most important metals (Arndt et al., 2017). They typically exhibit a spatial and temporal association with shallow, porphyritic or variably-textured intrusions with intermediate to felsic compositions (Candela & Piccoli, 2005; Seedorff et al., 2005). Many of these intrusions are connected to parental magma reservoirs at ~5 to ~15 km depths (Sillitoe, 2010; Audétat & Simon, 2012), which are multiphase and constructed incrementally over several millions of years (e.g. Chelle-Michou et al., 2014). A wealth of evidence has revealed that water, sulfur and metals within ore deposits were derived from these reservoirs by magma degassing (Hedenquist & Lowenstern, 1994; Candela, 1997; Richards, 2003; Sillitoe, 2010; Audétat & Simon, 2012). Field observations in combination with numerical simulations, suggest that a magma reservoir with volumes of $100 \, km^3$ or less can provide enough hydrothermal fluids to form an economic porphyry deposit (Cline & Bodnar, 1991; Cathles & Shannon, 2007; Chelle-Michou et al., 2017), and fluid exsolution can concentrate metals significantly (e.g. Zajacz et al., 2008; Audétat, 2019). In addition to their oxidized, hydrous and S-rich properties (Richards, 2003; Candela & Piccoli, 2005; Chambefort et al., 2008; Simon & Ripley, 2011), the parental magmas associated with mineralization in some tectonic settings have high Sr/Y ratios (Wang et al., 2006a, 2006b; Hou et al., 2009, 2015; Richards, 2011; Chiaradia et al., 2012).

Although magmatic-hydrothermal ore deposits have received much attention and are among the best understood ore deposit types, answers to some outstanding questions remain elusive. High magmatic water contents are essential for the formation of magmatic-hydrothermal ore deposits ($> \sim 4 \, wt \%$; Sillitoe, 2010), because fluid saturation and subsequent exsolution are the most important processes in metal endowment (Hedenquist & Lowenstern, 1994; Candela, 1997; Candela & Piccoli, 2005; Zajacz et al., 2008; Audétat & Simon, 2012). This concept is in agreement with the common association between porphyry deposits and arc magmas, which have average primitive water contents of ~4 wt % (Plank et al., 2013). However, a number of magmatic-hydrothermal ore deposits have also been described in association with magmatic systems where

the primitive melts have low H_2O contents, such as the Climax-type porphyry Mo deposits that are located in intraplate rift environments (e.g. Ludington & Plumlee, 2009; Audétat, 2015). In contrast to subduction zones (e.g. Zellmer et al., 2015), primitive magmas in other tectonic settings, such as intraplate and back-arc basins typically have relatively low H_2O contents (Wallace et al., 2015). A key question then arises as to how magmas become fertile for ore deposit genesis within such initially water-poor tectono-magmatic settings. Accurate measurement of dissolved H_2O concentrations in magmas associated with ore-forming systems is challenging. Analysis of mineral melt inclusions is a powerful method in such studies (e.g. Audétat, 2015). However, in some cases, melt inclusion data must be treated with caution, because exchange of H_2O and some trace elements between melt inclusions and their host magmas can occur through diffusion (e.g. Portnyagin et al., 2008; Rottier et al., 2017), particularly for samples with long residence times at magmatic temperatures. Thermodynamic calibrations may provide the ability to track the evolution of water in such cases (e.g. Waters & Lange, 2015), because the mineral components used to determine H_2O contents diffuse very slowly and thus are considered to remain unmodified after crystallization (e.g. Costa et al., 2003). Here, we present a quantified petrologic reconstruction of the transcrustal magmatic system associated with skarn-porphyry Cu–Fe–Au mineralization in the Edong district, China, paying particular attention to the evolution of magmatic H_2O contents. Igneous rocks in the Edong district and neighbouring areas are conventionally regarded as the products of an intraplate, extensional environment (e.g. Wang et al., 2004; Li et al., 2008; Hou et al., 2013; Pirajno & Zhou, 2015; Zhou et al., 2015). Accordingly, the district is an excellent location for the study of ore-forming magmatic processes in initially water-poor systems and to resolve the key question of how fertile magmas are generated within initially water-poor intraplate environments.

GEOLOGICAL BACKGROUND

The Edong district is located on the northern margin of the South China Block (Fig. 1), which consists of the Yangtze and Cathaysia Cratons, which are juxtaposed along the Jiangshan–Shaoxing fault (e.g. Hou et al., 2013). Large-scale, Late Mesozoic magmatic flare-ups

occurred in the South China Block (Zhou & Li, 2000; Hou *et al.*, 2013; Li *et al.*, 2013). In general, most igneous rocks near the coastline are granites and rhyolites, with minor andesitic rocks, and their origin has been interpreted as a result of subduction of the Paleo-Pacific plate (Zhou & Li, 2000; Li & Li, 2007). Far from the coastline and inboard from the direction of late Mesozoic subduction (Li & Li, 2007), there are seven similarly-sized Early Cretaceous volcano-plutonic complexes (mainly 144–120 Ma) near the Yangtze River, including the Edong district (e.g. Wang *et al.*, 2006*b*; Mao *et al.*, 2011; Li *et al.*, 2013; Wang *et al.*, 2013; Zhou *et al.*, 2015). They show a clear spatial association with the Yangtze River fault (Fig. 1; Chang *et al.*, 1991). Several geodynamic models have been invoked for the origin of these volcano-plutonic complexes, including partial melting of subducted mid-ocean ridge (e.g. Sun *et al.*, 2007; Ling *et al.*, 2009), partial melting of enriched lithospheric mantle (e.g. Li *et al.*, 2009, 2013), and delamination of dense lower crust (e.g. Wang *et al.*, 2004, 2006*a*, 2006*b*, 2007; Xu *et al.*, 2014; Zhu *et al.*, 2014; Jia *et al.*, 2016). Conventionally, igneous rocks in the Edong and neighbouring areas are regarded to have formed in an intraplate and extensional environment (e.g. Wang *et al.*, 2004; Li *et al.*, 2008; Hou *et al.*, 2013; Pirajno & Zhou, 2015; Zhou *et al.*, 2015). They display obvious differences to water-rich magmas and ore deposit types formed in subduction zones (Sillitoe, 2018). The volcanic rocks in the Edong district display a marked bimodal character (Xie *et al.*, 2011*a*), which is distinct from the intermediate-dominated volcanism above typical subduction zones such as the Central Andes (e.g. Wörner *et al.*, 2018).
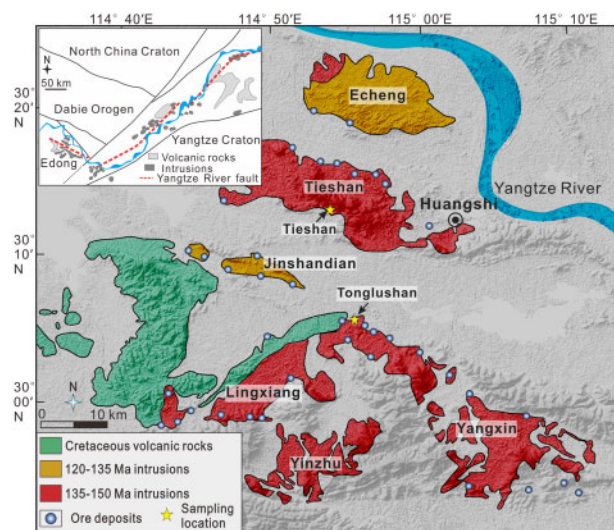
Several large plutons are exposed in the Edong district, with cogenetic volcanic rocks being mainly distributed in the western part of the area (Fig. 1). A statistical assessment of published geochronologic data (Supplementary Material; supplementary data are available for downloading at http://www.petrology.oxford journals.org) within the Edong district indicates the presence of two high-volume magmatic flare-ups at 145–135 Ma and 134–123 Ma, with peaks at 142 Ma and 127 Ma, respectively (Fig. 2). Most volcanic eruptions were simultaneous with the late magmatic flare-up, consisting of basalts and associated rhyolites (Xie *et al.*, 2011*a*). Intrusions in the Edong district and other plutonic complexes along the Yangtze River fault typically have high Sr/Y ratios (> 40; Wang *et al.*, 2004), which has been interpreted as being inherited from their
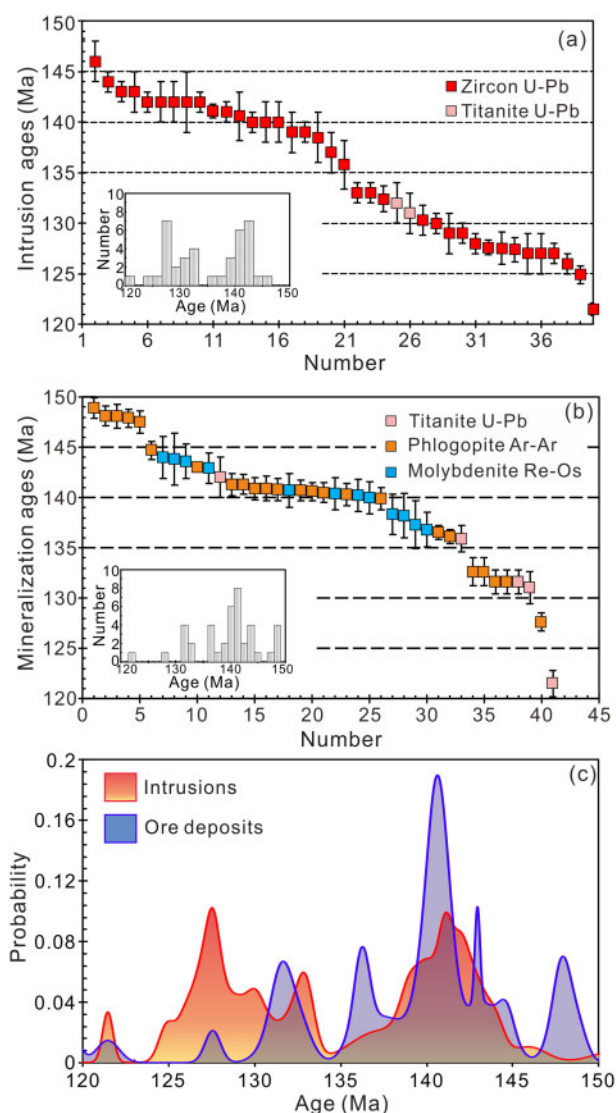

Fig. 1. Simplified geological map showing the distribution of Cretaceous intrusions, volcanics and magmatic-hydrothermal ore deposits in the Edong District, eastern China. Modified from Xie *et al.* (2011b) and Li *et al.* (2014). The inset map shows regional-scale characteristics and the location of the Edong District (modified from Li *et al.*, 2009). Yellow stars are the two deposits studied in this work.

Fig. 2. Ages of intrusions and ore deposits in the Edong district. (a) Zircon U–Pb ages for intrusions; (b) Mineralization ages dated by hydrothermal minerals; (c) Probability histogram of magmatic and hydrothermal ages. Data sources are provided in the Supplementary Material.

source region where garnet was present a residual phase during partial melting (Wang *et al.*, 2004, 2006*b*).

Extensive hydrothermal systems accompanied the Early Cretaceous magmatic activities in the Edong district. More than 70 magmatic-hydrothermal ore deposits have been found in this area, which has been one of the most productive Cu–Fe provinces in China (Li *et al.*, 2014, 2019). The principal alteration-mineralization types are skarn and porphyry styles. Dating of hydrothermal minerals from a number of deposits indicates that ore-forming events occurred episodically during the history of their associated magmatic activities, with a remarkable peak at 140 Ma (Fig. 2; Supplementary Material). Due to our focus on this metallogenic peak, intrusions associated with the mineralization in the Tieshan Fe–Cu skarn deposit and the Tonglushan Cu skarn deposit were sampled in this study.

The Tieshan deposit is situated on the southern margin of the Tieshan pluton (Fig. 1) and hosts six large orebodies at the contact between the quartz diorite and marbles, which contain combined 160 Mt Fe and 0·67 Mt Cu (Fig. 3a and b; Li *et al.*, 2014). The Tieshan quartz diorite has a zircon U–Pb age of 142 ± 3 Ma (Xie *et al.*, 2011b), and contains abundant mafic enclaves (Fig. 3c). Ar–Ar dating of mineralization-related phlogopite yielded a mineralization age of 140·9 ± 1·2 Ma (Xie *et al.*, 2007). The largest and richest ore deposit in the Edong district is the Tonglushan deposit (Duan & Jiang, 2017), which is located on the northern margin of the Yangxin plutonic complex (Fig. 1), with 1·08 Mt Cu, 60 Mt Fe, 70 t Au and 508 t Ag (Li *et al.*, 2014). Due to its identical age and proximity to the Tieshan deposit samples from the Tonglushan deposit were also analysed for comparison. The Tonglushan deposit consists of 12 orebodies that are mainly distributed at the contact zone between the quartz monzodiorite and marbles (Fig. 3d; Li *et al.*, 2014). Zircon U–Pb dating shows that the quartz monzodiorite has an age of 142 ± 1 Ma, and Ar–Ar dating of mineralization-related phlogopite indicates that the principal mineralization event in the Tonglushan deposit occurred at ~140 Ma (Li *et al.*, 2014).

Three main magmatic units were investigated in this study, including (1) mafic enclaves with a mineral assemblage of clinopyroxene, biotite, plagioclase, magnetite and titanite hosted by the Tieshan quartz diorite (TME; Fig. 4a). Five samples were collected for whole-rock analyses and the freshest one was selected for mineral chemistry analyses; (2) quartz diorites consisting of feldspar, amphibole, clinopyroxene, magnetite, quartz and titanite within the Tieshan deposit (TQD; Fig. 4b and c). Nine samples were collected for whole-rock analyses and the six of them were selected for mineral chemistry analyses; and (3) quartz monzodiorites with a mineral assemblage of feldspar, amphibole, quartz, magnetite and titanite in the Tonglushan deposit (TQM; Fig. 4d). Two samples were collected for whole-rock and mineral chemistry analyses.

METHODS

Analytical techniques

Whole-rock major element compositions were analysed by X-ray fluorescence spectrometry at Hubei Institute of Geology and Mineral Resource, with analytical errors less than 2%. The FeO contents were determined by wet chemical titration methods. Whole-rock trace element compositions were analysed with a Perkin-Elmer ELAN 6000 inductively coupled plasma source mass spectrometer (ICP-MS) at the State Key Laboratory of Isotope Geochemistry (SKLaBIG), Guangzhou Institute of Geochemistry, Chinese Academy of Sciences (GIG-CAS), following procedures similar to Li *et al.* (2002). Analytical precision is better than 2%. Sr and Nd isotopic analyses were carried out using a Finnigan MAT-262 mass spectrometer operated in a static multicollector mode at the Institute of Geology and Geophysics, Chinese Academy of Sciences, following the procedures described by Zhang *et al.* (2002). Sample powders were dissolved in Teflon capsules with HF+HNO$_3$ acids. Sr and Nd were separated by conventional cation-exchange technique. Total procedural blanks are <0·.5 ng for Rb and Sr, and ~50 pg for Nd and Sm. The La Jolla standard (recommended value = 0·511850) was used to monitor ^{143}Nd/^{144}Nd, with a value of 0·511854 ± 8 (2σ) determined in the lab. NBS987 (recommended value = 0·710245) was used as the standard for ^{87}Sr/^{86}Sr measurements, with a measured value of 0·710246 ± 9 (2σ) in this study. The measured Sr and Nd ratios are normalized to ^{86}Sr/^{88}Sr = 0·1194, ^{146}Nd/^{144}Nd = 0·7219, respectively.

Mineral major elements were analysed with a JEOL JXA 8230 electron probe micro-analyser (EPMA) using 15 kV accelerating voltage, 20 nA beam current and 1 μm probe diameter, at the Key Laboratory of Mineralogy and Metallogeny (KLMM) of GIG–CAS, and with a JEOL JXA 8100 Superprobe using 15 kV accelerating voltage, 20 nA beam current and 2 μm probe diameter at the SKLaBIG GIG–CAS, calibrated on natural and synthetic standards. The ZAF correction routine was used to reduce analytical results in both laboratories.

High resolution X-ray elemental intensity mapping was employed for imaging zoning patterns of plagioclase, using a JEOL JXA-8230 electron microprobe at the KLMM GIG–CAS. The operation conditions were 20 kV accelerating voltage, 100 nA beam current and 3 μm probe diameter.

Mineral trace element concentrations were measured using an ELEMENT XR (Thermo Fisher Scientific) ICP-SF-MS coupled with a 193-nm (ArF) Resonetics RESOlution M-50 laser ablation system in the SKLaBIG GIG–CAS. All LA-ICP-MS spots were overlapped to the analysed EMPA spots. The spot size was 33 μm, the laser repetition rate 5 Hz, and the pulse energy ~4 J cm^{-2}. A smoothing device (The Squid, Laurin Technic) was employed for smoothing the sample signal. For each analysis, 20 s gas blank collection (laser off) and 30 s sample signal detection (laser on) were recorded.
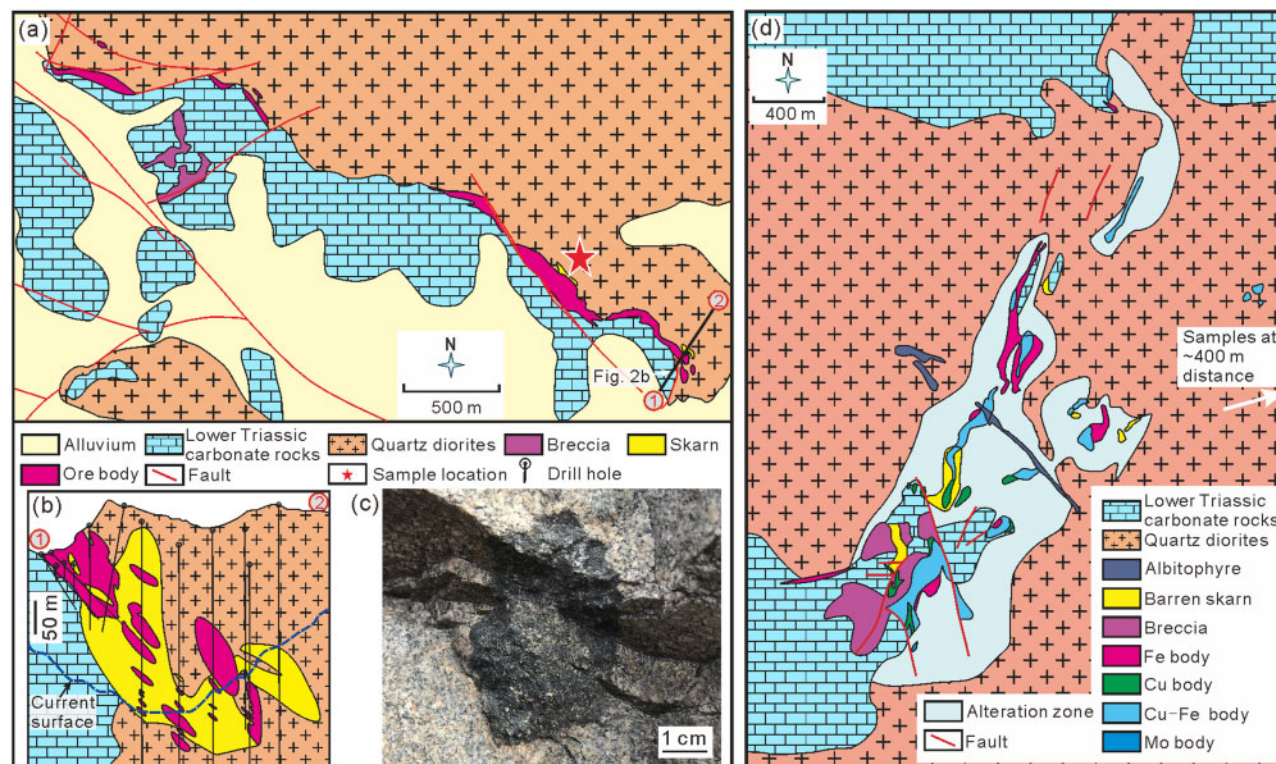
Fig. 3. (a) Geologic map of the Tieshan Fe–Cu deposit (from Zhu *et al.*, 2019); (b) Representative geologic section through the Tieshan deposit. Section line shown in Fig. 3a (from Zhu *et al.*, 2019); (c) Photograph of one of the studied mafic enclaves from Tieshan. The host is the Tieshan quartz diorite; (d) Geologic map of the Tonglushan deposit (from Li *et al.*, 2014).

Measurements were carried out in E scan mode. The BCR-2G, BHVO-2G and GSD-1G standards were used for the calibration. Pre-measured Si using EPMA was used as the internal standard element. The oxide molecular yield ($^{238}U^{16}O/^{238}U$ ratio) was less than 0.3%. The USGS reference glass TB-1G was analysed as an unknown, giving results that agreed within 10% with the reference values for most trace elements (Supplementary Material). More details of the experiment procedure and data reduction strategy can be found in Zhang *et al.* (2019).

RESULTS

Whole-rock compositions

The whole-rock major and trace element compositions of the TME, TQD and TQM are provided in Supplementary Table S1. The TME SiO_2 contents vary from 52·9 to 55·4 wt % and MgO contents from 3·70 to 6·25 wt %. The Mg# (molar Mg/[Mg + Fe_{total}] × 100) ranges from 48 to 57. The TME are markedly depleted in heavy rare earth element (HREEs) and enriched in light rare earth elements (LREEs). They have Sr/Y values of 33–168. The TQD have SiO_2 contents of 62·4–64·7 wt %, MgO contents of 1·42–1·92 wt %, and Mg# of 40–47. The majority of TQD are characterized by HREEs depleted signatures. They have Sr/Y values of 88–169. The TQM have SiO_2 contents (SiO_2 = 62·6–63·7 wt %)

similar to those of the TQD. They have MgO contents ranging from 0·86 to 1·44 wt %, with Mg# varying from 26 to 38. They are also characterized by enrichment in LREEs and depletion in HREEs, with Sr/Y values of 54–56.

All samples from the Tieshan and Tonglushan deposits are characterized by crustal Sr–Nd isotopic compositions (Supplementary Table S2). The TME define a range of ($^{87}Sr/^{86}Sr)_i$ ratios from 0·7064 to 0·7067 and a range of $\varepsilon_{Nd(t)}$ from -6·8 to -8·2, and the TQD ($^{87}Sr/^{86}Sr)_i$ ratios vary from 0·7067 to 0·7073, and $\varepsilon_{Nd(t)}$ from -10·1 to -8·3. Only one sample from the TQM has been analysed, with ($^{87}Sr/^{86}Sr)_i$ ratios of 0·7066 and $\varepsilon_{Nd(t)}$ of -6·9.

Mineral major and trace element compositions

All the mineral major and trace element analyses presented here can be found in the Supplementary Material of this study.

Plagioclase

Plagioclase is the dominant phase in the three main magmatic units within the Tieshan and Tonglushan deposits, and crystals are typically euhedral with lengths ranging from 300 to 2000 μm (Fig. 5). Some smaller, anhedral crystals are also present. BSE images show that the plagioclase crystals within the TME are homogeneous in chemical compositions (Fig. 5a and b).
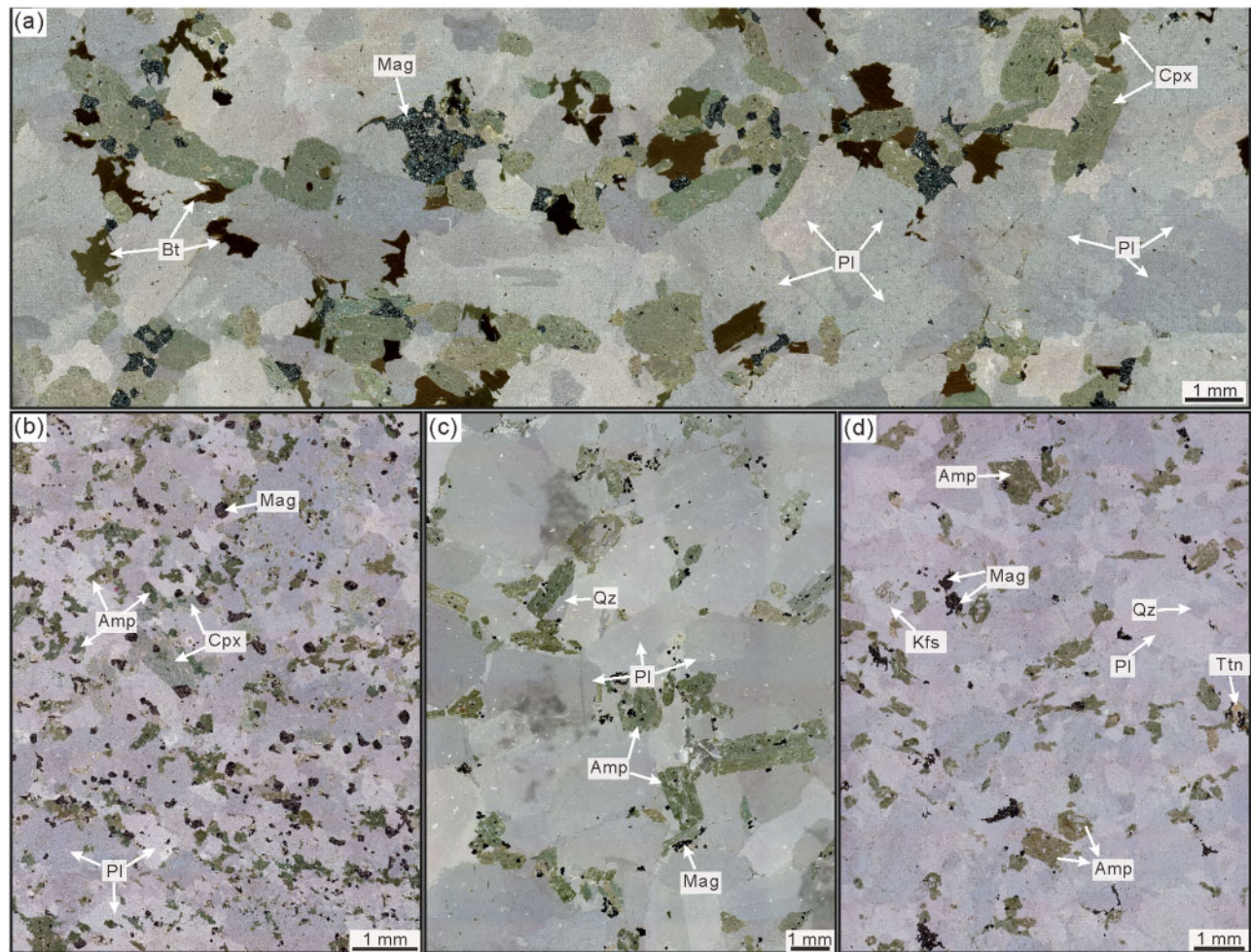
Fig. 4. Photographs of the three magmatic units investigated in this study. (a) a mafic enclave with a mineralogy of clinopyroxene, biotite, plagioclase, magnetite and titanite hosted by the Tieshan diorite; (b) and (c) the Tieshan quartz diorite with a mineralogy of feldspar, amphibole, clinopyroxene, magnetite, quartz and titanite within the Tieshan deposit; (d) the Tonglushan quartz monzo-diorite in the vicinity of the Tonglushan deposit, with a mineralogy of feldspar, amphibole, quartz, magnetite and titanite. Mineral abbreviations: Pl, plagioclase; Cpx, clinopyroxene; Bt, biotite; Mag, magnetite; Amp, amphibole; Qz, quartz; Kfs, K-feldspar; Ttn, titanite.

In contrast, the grains in the TQD and TQM commonly display normal zoning or oscillatory zoning (Figs. 5f and h). Variations of plagioclase compositions are shown in Figs 6a–8. Plagioclase major and trace element compositions are presented in Supplementary Table S3. Although the TME have more mafic whole-rock compositions than their host TQD, most of the TME plagioclases exhibit anomalously low An contents varying from An_{19} to An_{26} (the average = $An_{23 \pm 1}$, n = 42; Figs 6a and 7), high SiO_2 contents (61·3–64·2 wt %; Fig. 7a), low Al_2O_3 contents (21·3–23·5 wt %; Fig. 7b), and high FeO_T contents (0·20–0·38 wt %; Fig. 7c), with trace element concentrations in the range of 3617–4367 ppm Sr (the average = 3803 ± 161 ppm, n = 37; Fig. 8a), 548–1304 ppm Ba (average = 922 ± 201 ppm, n = 31; Fig. 8b), and 2791–7171 ppm K (average = 3860 ± 856 ppm, n = 32; Fig. 8c). Setting aside the compositional zoning within a single crystal, most of the TQD plagioclases are characterized by a wide range of compositions, with An contents from An_{11} to An_{44} (average = $An_{23 \pm 7}$, n = 202; Figs 8a and 7) and Sr concentrations from 1396 to 4927 ppm (the average = 2833 ± 927 ppm, n = 84; Fig. 8a), Ba contents from 80.0 to 1490 ppm (the average = 626 ± 405 ppm, n = 82; Fig. 8b). Traverses through individual TQD plagioclase crystals show that the cores are An-rich (Fig. 9a–c), typically varying from about An_{20} to An_{40}, and they are in equilibrium with the TQD whole-rock compositions, as evidenced by the Ab–An exchange coefficient $K_D(An–Ab)^{plagioclase–liquid}$ of 0·20–0·39 (Putirka, 2008). The TQD plagioclase rims are narrow (Fig. 9a and c) and have low An values (An_{10} to An_{20}). Plagioclase grains in the TQM commonly show normal zoning (Fig. 9d) and have relatively high An contents from An_{23} to An_{58} (average = $An_{38 \pm 11}$, n = 54; Figs 6a and 7), with Sr and Ba concentrations in the range of 1071–2752 ppm (average = 1884 ± 439 ppm, n = 18; Fig. 8a) and 138–671 ppm (average = 416 ± 173 ppm, n = 18; Fig. 8b), respectively.

Clinopyroxene

Clinopyroxene is another common phase in the TME (Fig. 4a). Most grains are euhedral or subhedral, with sizes ranging from 100 to 1000 μm in length. There is no visible zoning in the BSE images (Fig. 5a and b). Clinopyroxene major and trace element compositions are reported in Supplementary Table S4. The TME clinopyroxene compositions span a narrow range and most crystals are diopsidic ($Wo_{48–50}En_{37–42}Fs_{9–14}$) with Mg# varying from 71 to 79 (Figs 6b and 7), having low SiO_2 contents (50·7–53·4 wt %; Fig. 7d), high Al_2O_3 contents (1·57–3·76 wt %; Fig. 7e) and Na_2O contents (0·78–1·09 wt %; Fig. 7f). Most crystals are in equilibrium with the TME whole-rock compositions, based on Fe–Mg exchange coefficients $K_D(Fe–Mg)^{clinopyroxene–liquid}$ of 0·26–0·28, which match the equilibrium ranges of 0.27 ± 0.03 recommended by Putirka (2008). Their normalized REE patterns display enriched LREEs and depleted HREEs (Fig. 10a), with relatively high contents of some trace elements (e.g. Sr = 107–267 ppm, Zr = 118–205 ppm, V = 156–222 ppm; Fig. 8d and e). Most of the TQD clinopyroxene grains are smaller (100 to 500 μm) than the TME clinopyroxenes (Fig. 4b). They are diopside showing a narrow range in compositions ($Wo_{47–49}En_{36–38}Fs_{14–17}$; Fig. 6b) with Mg# varying from 70 to 74 (Fig. 7). The Fe-Mg exchange coefficients $K_D(Fe–Mg)^{clinopyroxene–liquid}$ (0·24–0·27) indicate that most of the TQD clinopyroxene are in equilibrium with the TQD whole-rock compositions. Listric-shaped chondrite-normalized REE diagrams show relative depletions in HREEs with respect to LREEs (Fig. 10b). The TQD clinopyroxenes have relatively low concentrations of some trace elements (e.g. Sr = 19·7–58·4 ppm, Zr = 9·2–87·7 ppm, V = 89·0–131 ppm; Fig. 8d and e). No clinopyroxene has been found in the TQM.

Amphibole

Amphibole is one of the dominant mineral phases in the TQD and TQM (Fig. 4b–d), but no amphibole crystals have been found in the TME. According to the classification of Leake *et al.* (1997), the TQD amphiboles are magnesiohornblende, with a small amount of actinolitic amphibole (Fig. 6c). Amphibole major and trace element compositions are summarized in Supplementary Table S5. Texturally, some of the TQD amphibole crystals are idiomorphic and other grains are anhedral (Figs 4b and c). The Mg#'s of idiomorphic amphiboles (average Mg# = 68 ± 3, n = 85) are slightly higher than those of subhedral crystals (average Mg# = 66 ± 2, n = 43; Fig. 7g and h). The chondrite-normalized REE patterns of the TQD amphiboles are characterized by LREEs enrichments over HREEs, with negative Eu anomalies (Fig. 10c). The compositions of the TQD amphibole cover a large range in regard to Sr (18·1 to 151 ppm; Fig. 8g), Zr (14·0 to 102 ppm), V (110 to 256 ppm) and Zn (109 to 395 ppm). The TQM amphiboles show a relatively narrow range of major element compositions (average Mg# = 69 ± 3, n = 46).

Compared with the TQD, amphibole crystals in the TQM have similar, but elevated REEs contents. On normalized REE profiles, they are enriched in LREEs and depleted in HREEs, coupled with negative Eu anomalies (Fig. 10d). The TQM amphibole grains have narrow ranges in composition for some trace elements (e.g. Sr = 9·2–32·9 ppm (Fig. 8g), Zr = 14·8–38·8 ppm, V = 120–214 ppm and Zn = 125–220 ppm).

A wealth of intensive parameters and information can be obtained using amphibole-only compositions (e.g. Barnes *et al.*, 2016, 2019). Multiple thermodynamic calibrations depending on single-amphibole compositions were utilized to estimate their crystallization conditions (Ridolfi *et al.*, 2010; Putirka, 2016). Given the test by Erdmann *et al.* (2014), oxygen fugacity and temperature were calculated using the Ridolfi *et al.* (2010) method (Eq. 1 and Eq. 2), and the equations (Eq. 5 and Eq. 10) from Putirka (2016) were employed to estimate temperature and equilibrium melt SiO_2 contents. The full range of temperature, oxygen fugacity and equilibrium melt SiO_2 contents of the amphiboles are illustrated in Fig. 11. Calculated temperatures from the above two independent methods define a near 1:1 correlation line (Fig. 11a), confirming that hornblende-only thermometers are a robust means to determine crystallization temperatures. Model temperatures of the TQD and TQM amphiboles using the Putirka (2016) method cover a range of 695–801 °C and 725–809 °C (Fig. 11a; Table 1), respectively. The TQD and TQM amphiboles record a continuous span in oxygen fugacity from $\Delta NNO = 1·0–2·2$ and 1·0–2·5 (Fig. 11b; Table 1), respectively. Equilibrium melts of the TQD amphiboles have SiO_2 contents of 69·9 ± 3·6 to 75·8 ± 3·6 wt % and those of the TQM span a range of 72·4 ± 3·6 to 75·2 ± 3·6 wt % (Fig. 11c).

DISCUSSION

Reconstruction of the magma plumbing system beneath the Tieshan deposit

Additional mineral-based thermodynamic calibrations provide quantitative estimates of intensive parameters. The incorporation of jadeite ($NaAlSi_2O_6$) into clinopyroxene is strongly pressure-sensitive and Al in clinopyroxene has very slow diffusivities, so that the clinopyroxene-liquid barometry is one of the widely used thermobarometers (Putirka, 2008). Using an extensive experimental dataset, Neave & Putirka (2017) developed an accurate clinopyroxene-liquid barometer suitable for hydrous and anhydrous magmas at crustal pressures. This clinopyroxene-liquid thermobarometry was applied in this study because the TME and some of the TQD samples contain clinopyroxene, whereas clinopyroxene is absent in the TQM. In order to obtain robust results, several key factors were assessed before performing calculations, following the scheme emphasized in the original thermobarometry study (Neave & Putirka, 2017). We employed two criteria to exclude
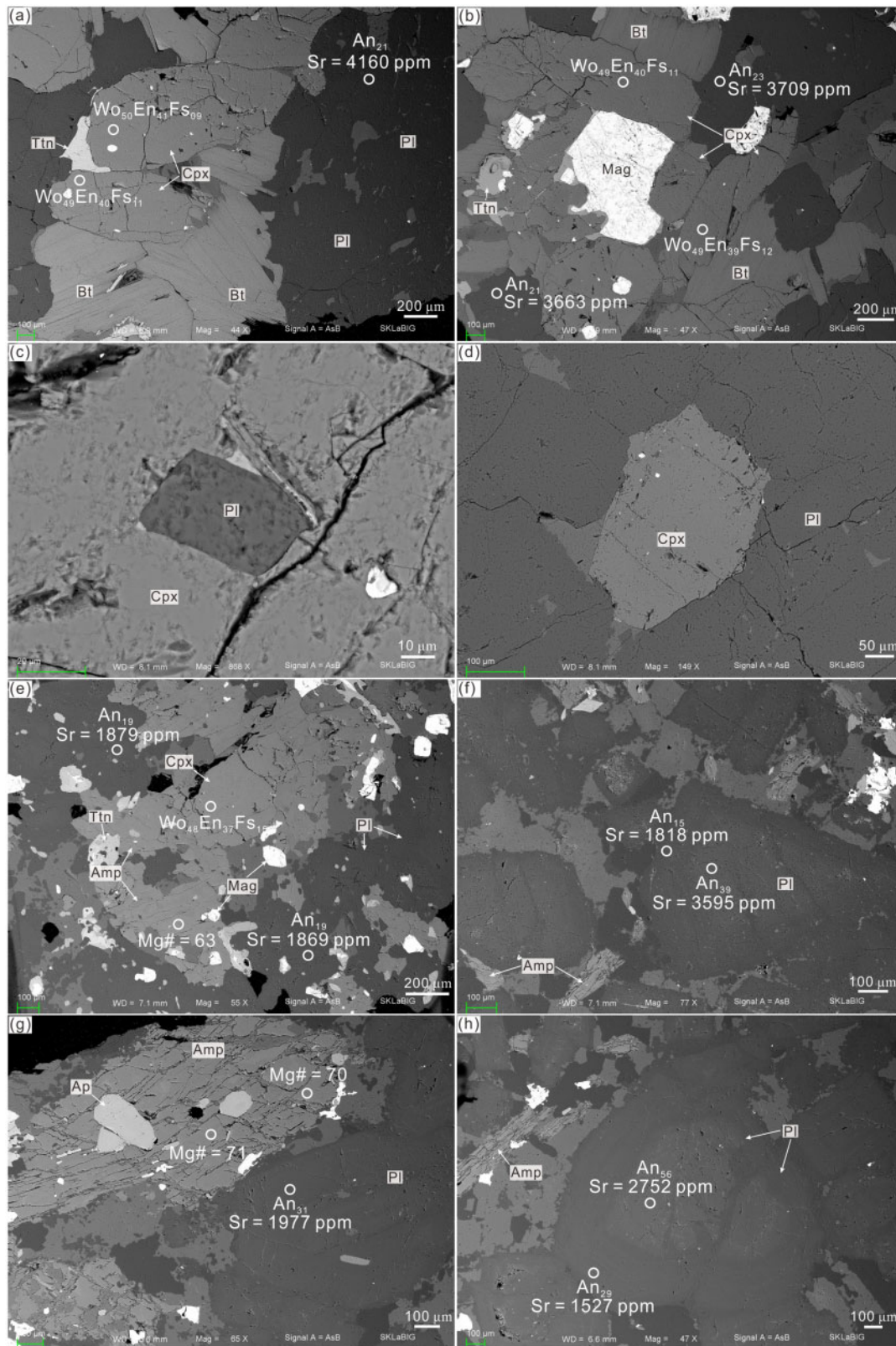
Fig. 5. Representative backscattered (BSE) images of the three main magmatic units. (a) and (b) the Tieshan mafic enclave; (c) idiomorphic plagioclase inclusion in the TME clinopyroxene; (d) idiomorphic clinopyroxene inclusion in the TME plagioclase; (e) and (f) The Tieshan quartz diorite; (g) and (h) The Tonglushan quartz monzodiorite. Mineral abbreviations: Pl, plagioclase; Cpx, clinopyroxene; Bt, biotite; Mag, magnetite; Amp, amphibole; Qz, quartz; Kfs, K-feldspar; Ttn, titanite; Ap, apatite.
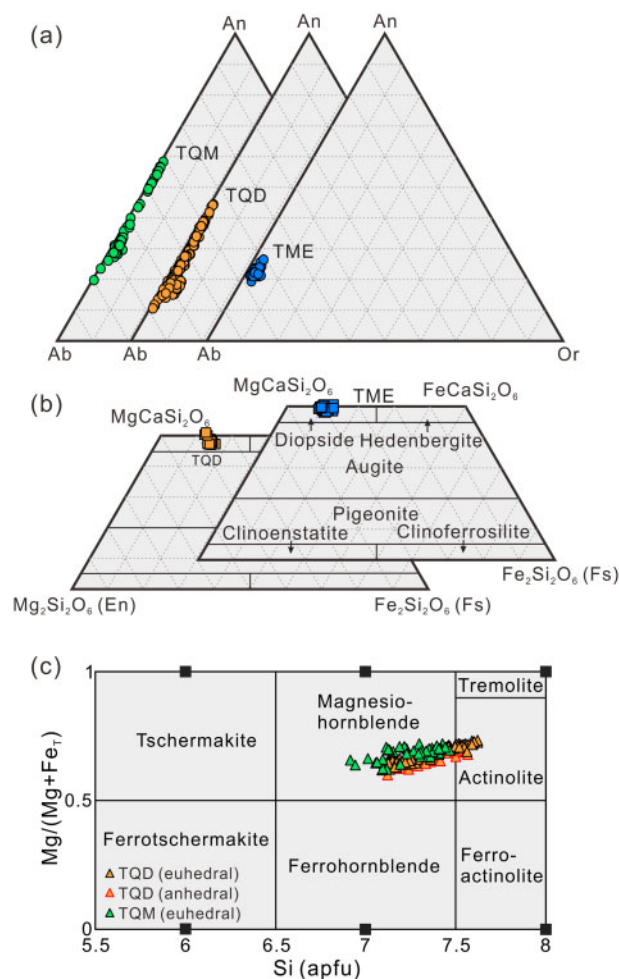
Fig. 6. Compositions of minerals in the Tieshan and Tonglushan samples. (a) Plots of plagioclase compositions on the Ab–Or–An ternary diagram; (b) Plots of clinopyroxene compositions on the En–Fs–Wo ternary diagram. Classification and nomenclature according to the scheme of Morimoto (1988); (c) Variation of amphibole compositions (after Leake *et al.*, 1997).

The TME clinopyroxenes record temperatures from 1043 to 1103 °C and pressures from 454 to 913 MPa. In contrast, the TQD clinopyroxenes give temperatures from 949 to 1009 °C and pressures from 190 to 590 MPa. Although individual pressure estimates have relatively large uncertainties (Fig. 12b), the TME and TQD clinopyroxenes exhibit tight clustering at means of 697 MPa (MSWD, mean square of weighted deviations = 0.49; n = 58) and 349 MPa (MSWD = 0.45; n = 33), with standard deviations of 98 and 90 MPa, respectively. These standard deviations are less than the model error of 140 MPa, which is the limit of the precision of the Jd-liquid reaction (Neave & Putirka, 2017). Combined with the MSWD values, the observed pressure ranges thus are more likely to represent the uncertainty inherited from the barometric calculations, rather than a wide range in depths. On that basis, the limited vertical pressures appear to record the sites of prolonged storage and cooling. In this case, the TME clinopyroxenes crystallized in the deep crust (at about 26 ± 3 km depth), and the TQD clinopyroxenes formed in the upper crust (at about 13 ± 3 km depth).

The bimodal distributions of magma storage pressures of the samples potentially provide an opportunity to explore the chemical and physical evolution that occurred in the transcrustal magma plumbing system beneath the Tieshan deposit. However, there are several possible origins of the TME, including (1) fragments of wall rock that were incorporated into the TQD; (2) recycled cumulates from the floor of magma chamber; (3) mafic globules after magma mixing or mingling; (4) crystallized materials from a deep, connected, magma chamber. Fragments of wall rock commonly have angular or irregular shapes (e.g. Zhou *et al.*, 2020*a*), but the TME are rounded (Fig. 3c). The significant differences in crystallization pressure between the TME and TQD exclude the possibility that the TME are recycled cumulates from the floor of the TQD magma chamber. In fact, mafic enclaves are common in granitoid plutons, and are generally interpreted as globules of magma mixing or mingling after mafic injection (e.g. Wiebe *et al.*, 2004). It is noteworthy that mafic enclaves derived from mafic injection are usually finer-grained than their host because of temperature difference-induced quenched crystallization (Vernon, 2004) but the TME are relatively coarse-grained (Figs 3c and 4a). Therefore, the TME most likely represent the crystallized materials from a deep-seated, connected magma chamber. Clinopyroxene and plagioclase are the two most abundant mineral phases in the TME and both commonly as inclusions within the other minerals (Fig. 5c and d). In addition, the TME clinopyroxene and plagioclase crystalized simultaneously (Fig. 5c and d), so that the TME had reached high crystallinity when they were captured by the TQD magmas. The attainment of Fe–Mg exchange equilibrium between the TME whole-rock compositions and clinopyroxenes (Fig. 12a) suggests that the TME are unlikely to represent cumulates, but crystallized materials from the deep magma chamber. Most of the TQD plagioclase crystals
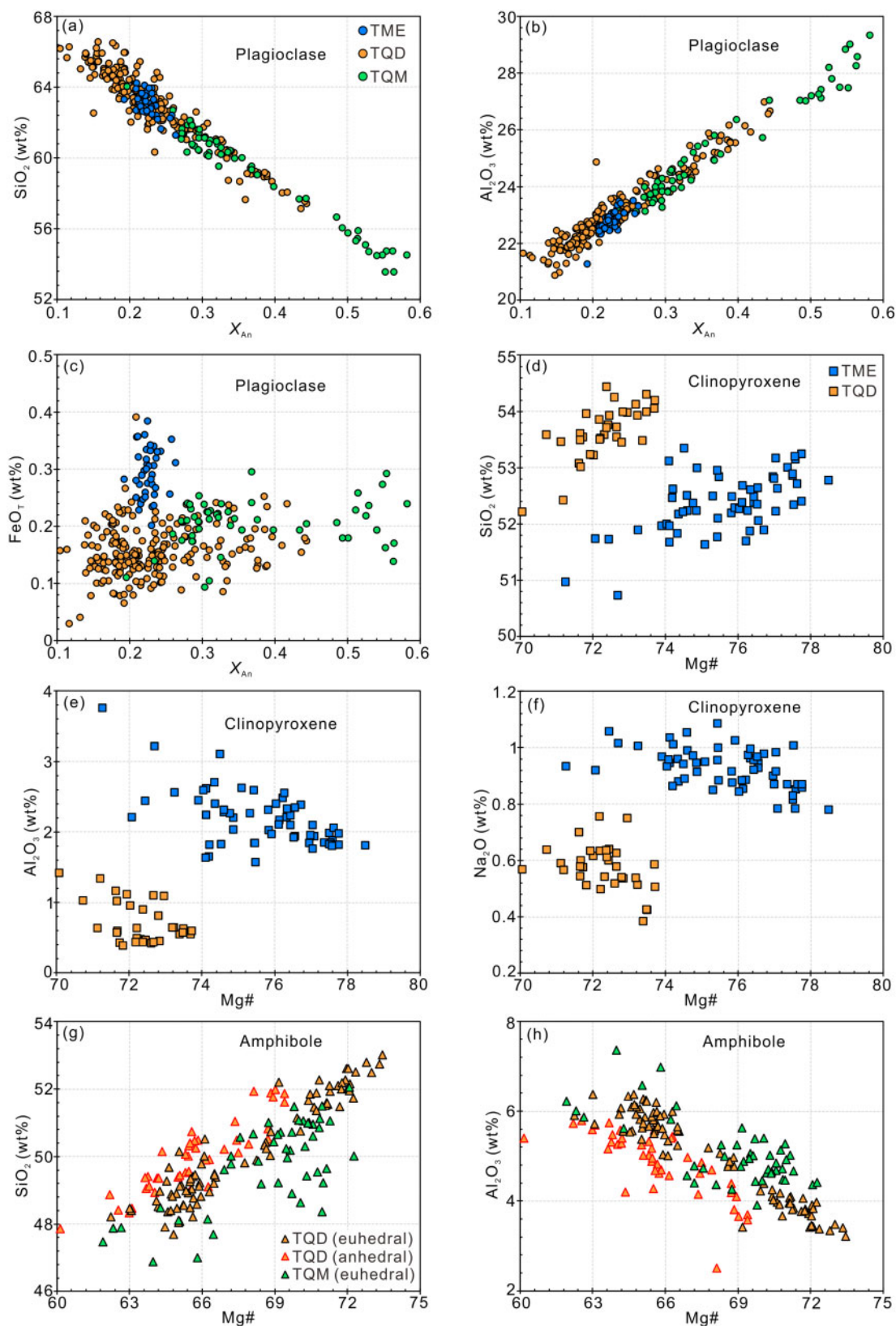
potential outliers in the mineral data set, avoiding the effects of analytical errors on thermobarometric calculations, i.e. the total number of cations (based on six-oxygen) varies within a range of 3.99–4.02, and jadeite (Jd) contents must be greater than 0.01. All mineral-based thermodynamic calibrations are developed on cases where chemical equilibrium between crystals and liquids was achieved. Therefore, identification of appropriate melts in equilibrium with the TQD and TME clinopyroxenes is critical before application. Here, the whole-rock compositions were used as the melt compositions, as supported by the Fe–Mg exchange coefficient, which was defined as $K_D(\text{Fe–Mg})^{\text{cpx-liq}} = [(X_{\text{Fe}}^{\text{cpx}} * X_{\text{Mg}}^{\text{liq}})/(X_{\text{Mg}}^{\text{cpx}} * X_{\text{Fe}}^{\text{liq}})]$. Clinopyroxene-liquid pairs that have K_D within a range of 0.28 ± 0.08 (Putirka, 2008) were regarded to be in a chemical equilibrium. Fig. 12a shows that the majority of TQD and TME clinopyroxenes are in equilibrium with the corresponding whole-rock compositions. The calculated temperatures and pressures are summarized in Fig. 12b and Table 1.

Fig. 7. Major element variation in plagioclase, clinopyroxene and amphibole. (a) SiO_2 of plagioclase vs X_{An}; (b) Al_2O_3 of plagioclase vs X_{An}; (c) FeO_T of plagioclase vs X_{An}; (d) SiO_2 of clinopyroxene vs Mg#; (e) Al_2O_3 of clinopyroxene vs Mg#; (f) Na_2O of clinopyroxene vs Mg#; (g) SiO_2 of amphibole vs Mg#; (h) Al_2O_3 of amphibole vs Mg#.
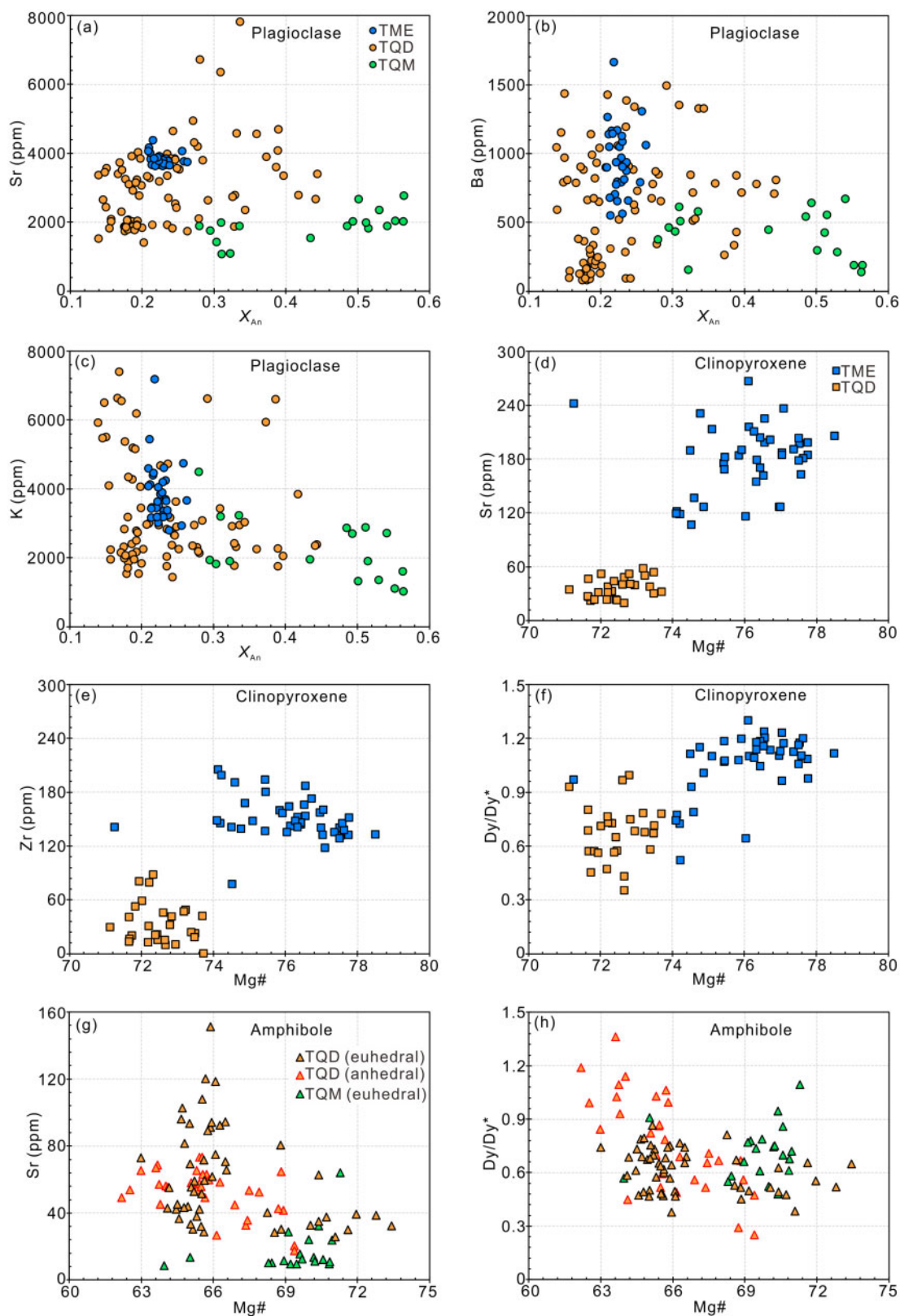
Fig. 8. Trace element variation in plagioclase, clinopyroxene and amphibole. (a) Sr of plagioclase vs X_{An}; (b) Ba of plagioclase vs X_{An}; (c) K of plagioclase vs X_{An}; (d) Sr of clinopyroxene vs Mg#; (e) Zr of clinopyroxene vs Mg#; (f) Dy/Dy* of clinopyroxene vs Mg#; (g) Sr of amphibole vs Mg#; (h) Dy/Dy* of amphibole vs Mg#.
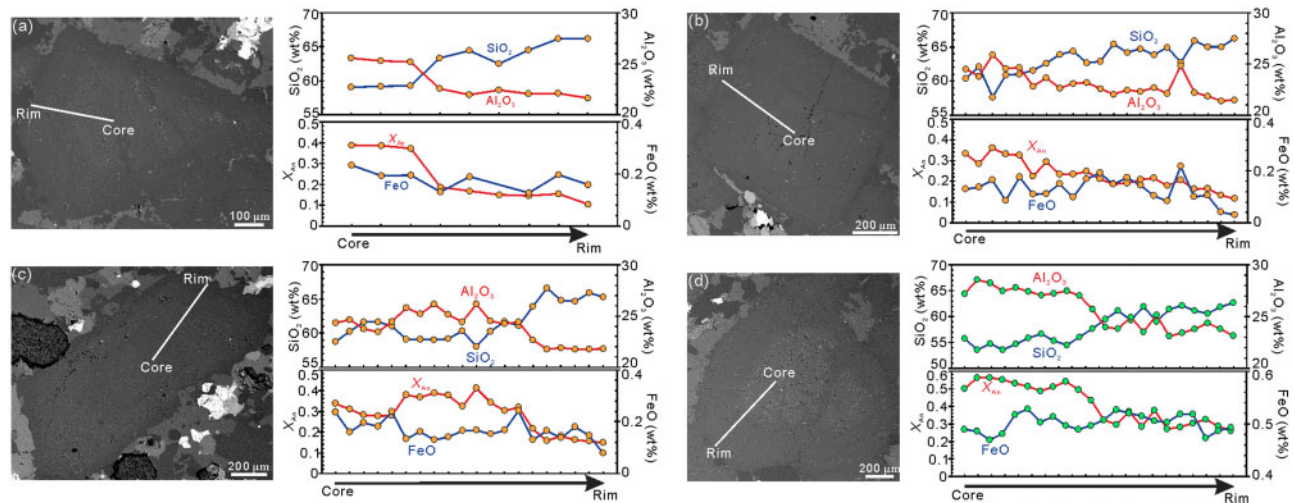
Fig. 9. Traverse analyses of zoned plagioclases from TQD and TQM. (a–b) Normal-zoned plagioclase from TQD; (c) Oscillatory-zoned plagioclase from TQD; (d) Normal-zoned plagioclase from TQM.
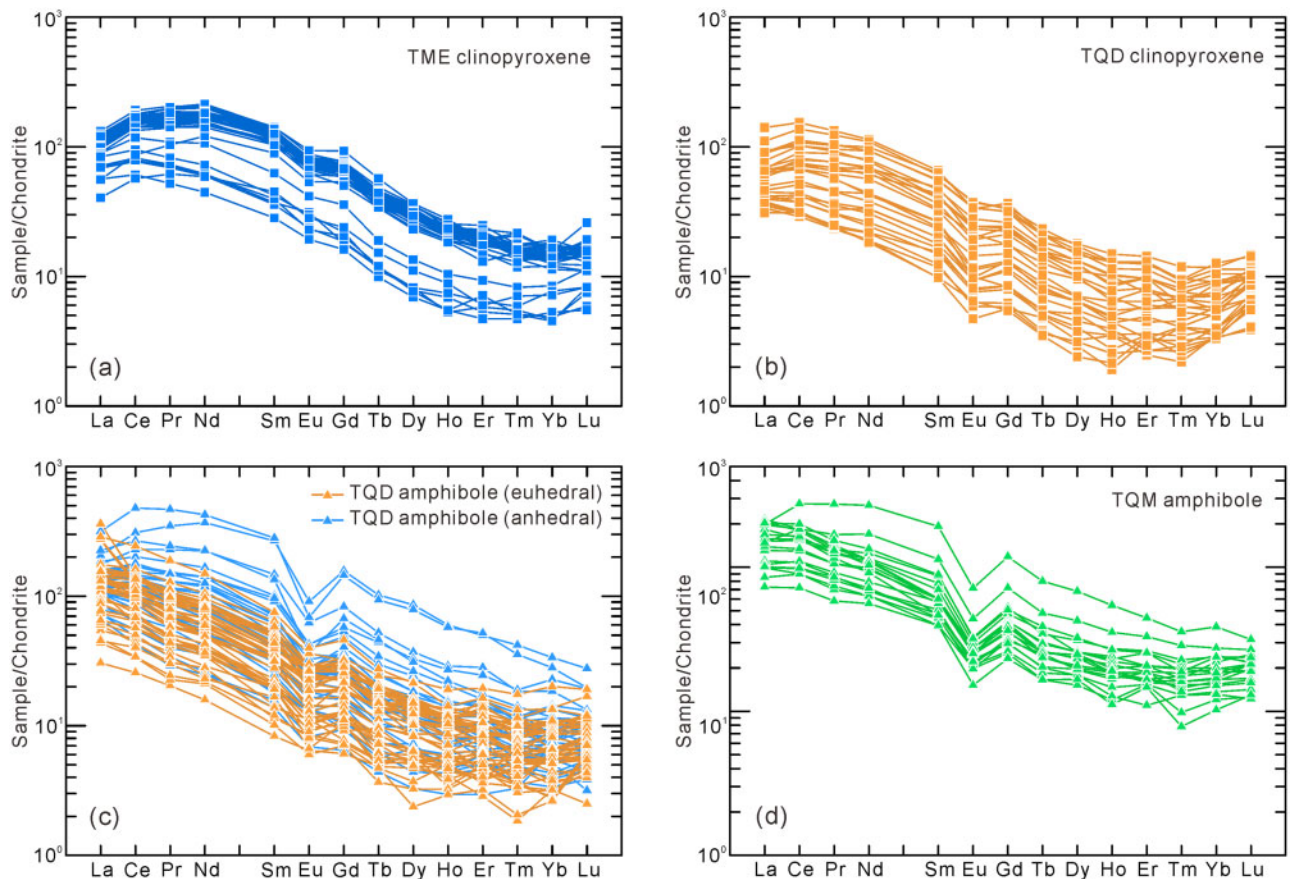

Fig. 10. Chondrite-normalized (Sun & McDonough, 1989) rare earth element patterns of clinopyroxenes and amphiboles. (a) Clinopyroxenes from one of the studied mafic enclaves from Tieshan. (b) Clinopyroxenes from the Tieshan quartz diorite. (c) Amphiboles from the Tieshan quartz diorite. (d) Amphiboles from the Tonglushan quartz monzodiorite.

are characterized by normal zoning with An-rich cores and more Ab-rich rims. A small proportion of the TQD plagioclase grains has a distinctive zoning pattern, which consists of a small, irregular corroded core, surrounded by normal oscillatory zoning (Fig. 14). The corroded portion has lower An contents (An_{24} to An_{27}) with high Na and low Ca, Al contents (Fig. 14b–d), showing an abrupt change in compositions toward the outer zones (Fig. 14a), in which An contents vary continuously from An_{44} to An_{11}, similar to the dominant plagioclase
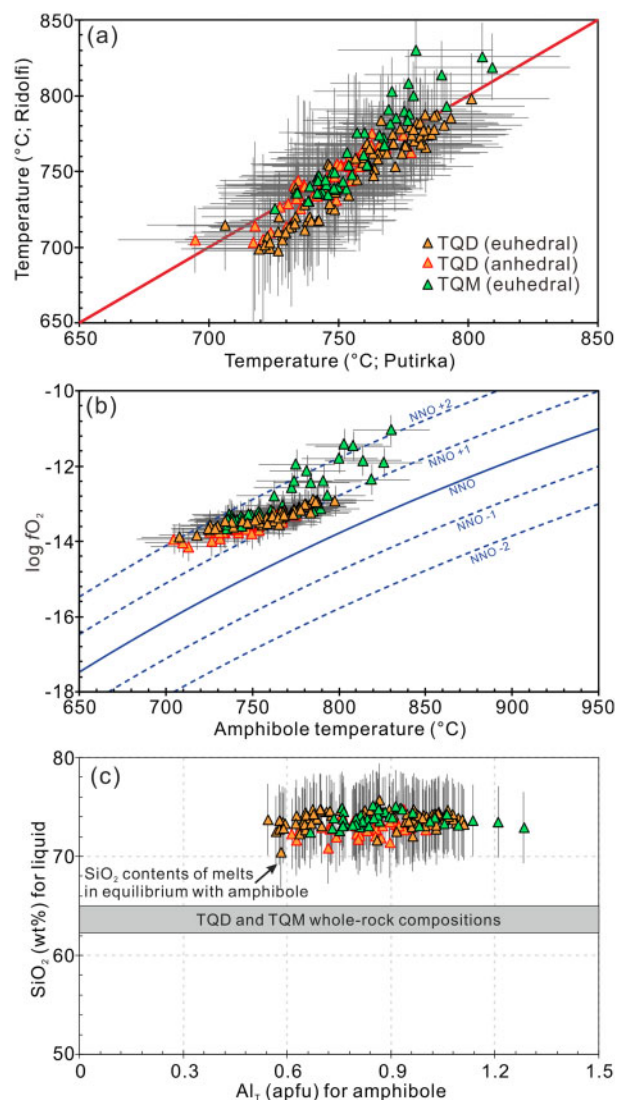
Fig. 11. Calculated temperature, oxygen fugacity, and SiO₂ contents of equilibrium melts using the TQD and TQM amphibole compositions. Equations 1 and 2 of Ridolfi *et al.* (2010) were used to calculate temperature and oxygen fugacity, and equations 5 and 10 from Putirka (2016) were employed to estimate temperature and equilibrium melt SiO_2 contents. The calibrations of the nickel–nickel oxide (NNO) buffer is taken from O'Neill & Pownceby (1993), using the average pressure of the TQD clinopyroxenes.

population in the TQD. Thus, the corroded cores are interpreted as inherited grains that crystallized at deeper levels, consistent with the common interpretation of such features (Vernon, 2004). More importantly, the TME plagioclases (mean = $An_{23 \pm 1}$; Figs 6a and 7) are compositionally identical to the corroded cores in some TQD plagioclases (mean = $An_{25 \pm 2}$; Fig. 14a), so the corroded cores were derived from the deep magma reservoir where the TME crystallized. Based on the above results and observations, we propose that the mineralization-related TQD are evolved products from a deep magma reservoir, which is intermediate in composition and may be equivalent to the TME in compositions. Therefore, a

simplified model of the magma plumbing system beneath the Tieshan deposit emerges where an intermediate magma reservoir at mid- to lower-crustal depths fed the construction of the Tieshan pluton and associated hydrothermal system.

Whole-rock trace element and Sr–Nd isotopic compositions also provide important information regarding the origin of melts that contributed to the development of the magmatic system. All magmatic rocks within the Tieshan and Tonglushan deposits show crustal Sr and Nd isotope signatures, including the TME samples (($^{87}Sr/^{86}Sr)_i$ = 0.7064–0.7067, $\varepsilon_{Nd(t)}$ = -6.8 to -8.2), the TQD samples (($^{87}Sr/^{86}Sr)_i$ = 0.7067–0.7073, $\varepsilon_{Nd(t)}$ = -10.1 to -8.3), and the TQM samples (($^{87}Sr/^{86}Sr)_i$ = 0.7066, $\varepsilon_{Nd(t)}$ = -6.9). It is noteworthy that the TMEs can be divided into two groups where one group is characterized by low MgO (3.70–4.02 wt %), Cr (9.00–46.0 ppm), Ni (16.5–28.2 ppm) but high Sr (2639–2759 ppm) contents and low $\varepsilon_{Nd(t)}$ (-7.8 to -8.2) and high Sr/Y (142–168) values and the other group has higher MgO (6.25 wt %), Cr (209 ppm), Ni (68.3 ppm) but lower Sr (785 ppm) contents and relatively high $\varepsilon_{Nd(t)}$ (-6.8) and lower Sr/Y (33) values. This indicates that the deep magma reservoir was heterogeneous in composition. Unlike subduction zones in which fluid-mediated melting is the dominant mechanism for the genesis of primitive magmas (e.g. Tatsumi, 1989; Hawkesworth *et al.*, 1993; Ulmer & Trommsdorff, 1995; Grove *et al.*, 2002), the origin of magmas within intraplate environments can be ascribed to diverse processes. A probable scenario for magma genesis in the East and North China during the Late Jurassic to the Early Cretaceous invokes a delamination event (e.g. Xu *et al.*, 2002; Gao *et al.*, 2004; Wang *et al.*, 2004, 2006b), which is an important process in the evolution of continental crust (see the review of Ducea *et al.*, 2015). If this was the case, then the two different groups of TMEs may be cogenetic but reflect different extents of interaction between melts from delaminated lower crust and mantle peridotite (e.g. Gao *et al.*, 2004; Wang *et al.*, 2004, 2006b). Alternatively, the two groups may represent magmas derived from different sources, i.e. high Mg melts are a result of partial melting of delaminated mantle and low Mg melts originated from partial melting of delaminated lower crust.

Tracking the evolution of water within the magma plumbing system

Primary objective of this study is to present an accurate picture of the evolution of H_2O within the magma plumbing system associated with the mineralization. Traditionally, analyses of melt inclusions trapped in minerals are the mainstay of such studies (e.g. Audétat, 2015). However, studies of melt inclusions may not be suitable for samples that undergo slow cooling and have long residence times at magmatic temperatures, such as the TME in this study, which crystallized in the hot deep crust (at about 26 km depth; Fig. 12b) and were subsequently carried to the upper crust by the TQD

Table 1: Summary of magmatic intensive parameters calculated from minerals

	T (°C) Range	T (°C) Mean	P (MPa) Range	P (MPa) Mean	H$_2$O (wt %) Range	H$_2$O (wt %) Mean	log$_{10}$ fO_2 Range	log$_{10}$ fO_2 Mean	ΔNNO Range	ΔNNO Mean
Tieshan mafic enclave (TME)										
Clinopyroxene	1043–1103[1]	1080 ± 17	454–913[1]	697 ±98						
Plagioclase					0.8–1.7[2]	1.0 ± 0.2				
Tieshan quartz diorite (TQD)										
Clinopyroxene	949–1009[1]	981 ± 12	190–590[1]	349 ± 90						
Plagioclase					2.1–2.8[2]	2.4 ± 0.2				
Amphibole	695–801[3]	753 ± 21			3.2–4.6[4]	3.9 ± 0.3	−12.9–14.1[4]	−13.4 ± 0.3	1.0–2.2[4]	1.4 ± 0.3
Tonglushan quartz monzodiorite (TQM)										
Amphibole	725–809[3]	759 ± 19			3.4–4.4[4]	3.9 ± 0.2	−11.0–13.7[4]	−12.9 ± 0.7	1.0–2.5[4]	1.7 ± 0.3

Calibrations: [1]Neave & Putirka, (2017); [2]Waters & Lange, (2015); [3]Equation 5 of Putirka, (2016); [4]Ridolfi *et al.*, (2010).
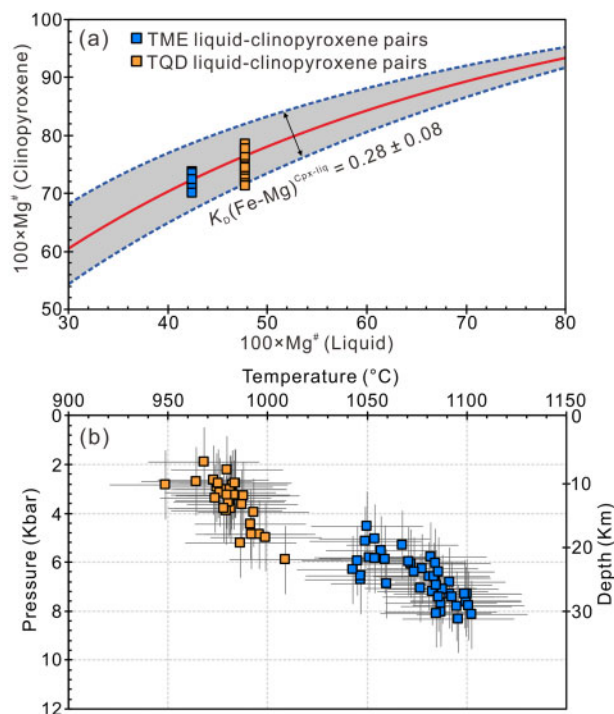

Fig. 12. (a) Tests of clinopyroxene-melt equilibrium. K_D values within a range of 0·28 ± 0·08 (Putirka, 2008) were regarded to signify chemical equilibrium. (b) *P–T* results of the Tieshan mafic enclaves and quartz diorite using the clinopyroxene-liquid thermobarometry (Neave & Putirka, 2017). The standard errors of estimate (SEE) are ± 140 MPa for pressures and ± 28 °C for temperatures.

magmas. Diffusive re-equilibration can easily be achieved in such cases, particularly for volatile components (e.g. Portnyagin *et al.*, 2008). Here, we employed multiple thermodynamic calibrations, including the plagioclase-liquid hygrometer and the amphibole hygrometer to track the evolutionary pathway of magmatic water contents within the magma plumbing system. Hygrometric equations in the above calibrations are mainly based on components with exceedingly sluggish diffusion rates, which are commonly considered to be unmodified after initial crystallization (e.g. Costa *et al.*, 2003).

Plagioclase-liquid hygrometers, based on the plagioclase-liquid exchange between anorthite and albite components, appears to be an effective and commonly-used method to determine magmatic H$_2$O contents (e.g. Putirka, 2008; Zellmer *et al.*, 2012; Wallace *et al.*, 2015; Rottier *et al.*, 2020). They have been updated using an expansive dataset and can be applied to a wide range of melt compositions, pressures and temperatures (Waters & Lange, 2015). However, application of this hygrometer requires that the magma temperature at the time plagioclase crystallizes has been accurately constrained, as it has strong effects on the results of hygrometric calculations. For example, if one takes the average whole-rock composition of the TQD and the pressure derived from clinopyroxene-liquid barometry the resultant H$_2$O contents increase by 0·9 wt % if temperature decreases by 50 °C. The presence of idiomorphic clinopyroxene inclusions in plagioclase and idiomorphic plagioclase inclusions in clinopyroxene (Fig. 5b and d) indicates that clinopyroxene and plagioclase grew simultaneously and thus should have similar crystallization temperatures. We employed the clinopyroxene-liquid thermobarometer (Neave & Putirka, 2017) and plagioclase-liquid hygrometer (Waters & Lange, 2015) to obtain clinopyroxene temperatures and magmatic water contents. Magmatic water contents should be known before attempting the clinopyroxene-liquid thermobarometer. This problem was solved iteratively using a combination of the clinopyroxene-liquid thermobarometer and plagioclase-liquid hygrometer. The results suggest that plagioclases crystallized from melts with 0·8 ± 0·4 to 1·7 ± 0·4 wt % H$_2$O in the case of TME and 2·1 ± 0·4 to 2·8 ± 0·4 wt % in the case of TQD (Fig. 13; Table 1). The amphibole hygrometer is another useful calibration to calculate magmatic water concentrations, although it does not have an accuracy comparable to the plagioclase-liquid hygrometer (Wallace *et al.*, 2015). The amphibole hygrometer employed here is mainly based on amphibole-only compositions (Ridolfi *et al.*, 2010), so there is no additional deviation created by constraining model parameters such as temperature, pressure and melt compositions. Application of this hygrometer results in

water content estimates that range from $3\cdot2 \pm 0\cdot4$ to $4\cdot6 \pm 0\cdot4$ wt % for the TQD and $3\cdot4 \pm 0\cdot4$ to $4\cdot4 \pm 0\cdot4$ wt % for the TQM (Fig. 13; Table 1).

Calculated magmatic H_2O contents can be employed in conjunction with other intensive variables to track the evolution of H_2O within the plumbing system. There is no compelling evidence supporting a genetic link between the Tieshan and Tonglushan magmatic systems, but they have nearly identical ages and occur in close proximity (Fig. 1). Therefore, the data from the Tonglushan deposit are shown for comparison. Considering crystallization conditions in terms of pressure, temperature and equilibrium liquid compositions, we recognized three critical stages during the evolution of H_2O within the plumbing system. At the earliest stage, magmas accumulate in the deep crust (at about 26 km depth beneath the Tieshan deposit) to form an intermediate magma reservoir with initial H_2O contents of 0·8–1·7 wt %, as recorded by the TME plagioclases. Our calculated H_2O contents are supported by the anomalously Ab-rich composition of plagioclase (An_{19-26}) in TME, which is significantly higher than that of common plagioclase in intermediate whole-rock compositions. At the same time, such low H_2O contents indicate that the Tieshan initial magmas are distinguished from arc magmas, which have elevated initial water contents with a global average of ~4 wt % (Plank *et al.*, 2013). Evolved melts derived from this deep crustal magma reservoir ascended and ponded in the upper crust (at about 13 km depth as indicated by clinopyroxene pressures), forming a magma body with an initial water content of 2·1–2·8 wt %, as indicated by the TQD plagioclases. Thus, the first enrichment of water in magmas can be attributed to the dynamics of the deep crustal magma reservoir, including continuous crystallization of anhydrous minerals and the concentration of H_2O in the residual melt (Boudreau, 2016). The shallow magma body, equivalent to the TQD in composition, had an extensive cooling ranging from clinopyroxene and plagioclase temperatures of 949–1009 °C down to amphibole temperatures of 695–801 °C. Amphibole
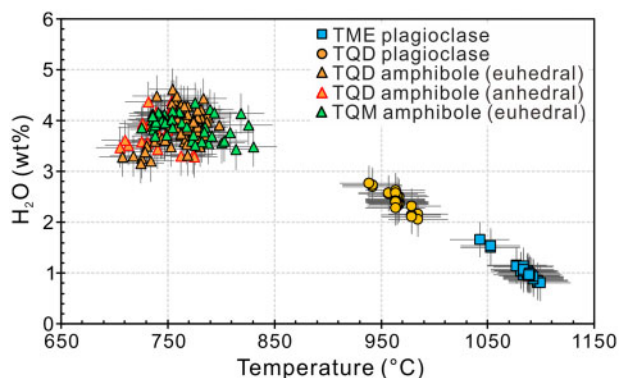

Fig. 13. Plot of calculated magmatic water contents versus temperatures, using the plagioclase-liquid hygrometer (Waters & Lange, 2015) and the amphibole hygrometer (Ridolfi *et al.*, 2010).

crystallized when the magma body reached high crystallinity, as evidenced by low crystallization temperatures and SiO_2-enriched melts in equilibrium with amphibole crystals (Fig. 11c). At this stage the system turned relatively H_2O-rich with water contents ranging from 3·2 to 4·6 wt %. In short, isobaric cooling of the shallow magma body gave rise to the second enrichment of H_2O in residual melts, ultimately leading to magmas that were fertile for mineralization (Sillitoe, 2010).

The western North American Climax-type porphyry Mo deposits are another important ore deposit type that formed from initially water-poor magmatic environments (Ludington & Plumlee, 2009). Unlike subduction-related porphyry Mo deposits, Climax-type deposits have high grades and are associated with fluorine-rich, high-silica rhyolite magmas in intraplate, rift settings (Carten *et al.*, 1993; Audétat & Li, 2017). Although primitive magmas in intraplate environments have low H_2O contents, the mineralizing melts associated with Climax-type deposits are rich in water (4–9 wt %; Audétat & Li, 2017), hence H_2O became concentrated during extreme fractionation (Audétat, 2015). From the perspective of water contents in primitive magmas, the Tieshan magmatism shows similarities to Climax-type porphyry systems. However, the Tieshan deposits are dominated by Cu–Fe whereas Mo is the primary commodity in Climax-type deposits (Ludington & Plumlee, 2009). We speculate that this different metal endowment can be ascribed to the capability of crystal–melt separation in shallow magma chambers. Due to slow separation rates and short thermal lifetimes, extraction of highly evolved interstitial melts from a shallow magma chamber is difficult. Only under some favorable set of condition, can rhyolitic interstitial melts be expelled to form crystal-poor high-SiO_2 rhyolites (e.g. Bachmann & Bergantz, 2004; Bachmann & Huber, 2019) and certain high-silica granites (e.g. Putirka *et al.*, 2014; Zhou *et al.*, 2020*b*). If efficient crystal–melt separation occurs, then the magmatic system preferentially generates porphyry Mo deposits (e.g. Audétat, 2015). In contrast, Cu and Fe endowments are commonly associated with intermediate intrusions, rather than high-silica magma bodies (Hedenquist & Lowenstern, 1994; Meinert *et al.*, 2005). Magmatic evolution at shallow crustal levels, however, will prevent the formation of economic Cu deposits (Chiaradia & Caricchi, 2017), because Cu is a compatible element during fractional crystallization (Audétat, 2019).

Constraining magmatic system evolution via trace element systematics

Further insights into the evolution of the Tieshan magma plumbing system can be obtained from mineral trace element systematics. Conventionally, the whole-rock trace element composition of igneous rocks provides fundamental clues to their origin and evolution. However, there has been an increasing recognition that
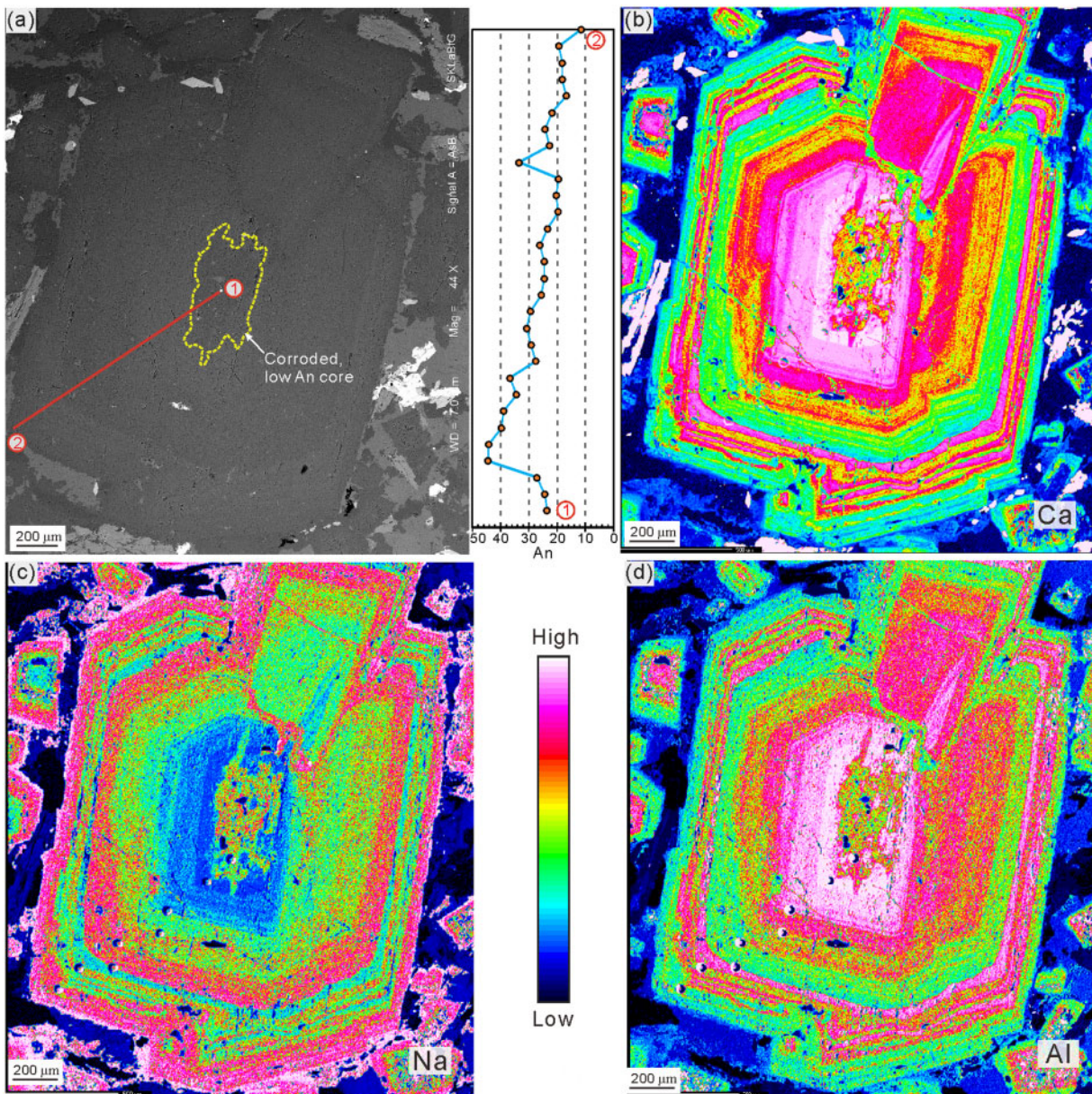
Fig. 14. (a) BSE image of a TQD plagioclase grain with a distinctive zoning pattern that consists of a small, irregular corroded core, surrounded by normal oscillatory zoning. (b) X-ray calcium (Ca) intensity map. (c) X-ray sodium (Na) intensity map. (d) X-ray aluminum (Al) intensity map.

crystals in shallow intrusions are rarely composed of a single crystal population (e.g. Jerram & Martin, 2008). The diversity of populations is attributed to a number of magmatic processes, rather than to only one crystallization event of the type responsible for the lower An cores within the TQD plagioclase reported in this study. Studies of mineral trace elements and their equilibrium melts, however, do commonly provide more detailed information about the range of magmatic processes that may be overlooked by whole-rock approaches. A particular challenge in the calculation of mineral equilibrium melts is that mineral-melt partition coefficients can vary significantly and are sensitive to temperature, pressure, melt and mineral compositions (e.g. Sun

et al., 2017), so application of a single experimental partition coefficient to natural samples has large uncertainties. Here, only trace elements with well-known partitioning behavior in a given phase were employed. For most trace elements, the partition coefficients can be predicted by the lattice strain model (Blundy & Wood, 1994). According to this model, the partition coefficients of trace elements between mineral and melt can be expressed as:

$$D_i^{Mineral-melt} = D_0 \exp\left[- \frac{4\pi E N_A}{RT} \left(\frac{r_0}{2}(r_0 - r_i)^2 - \frac{1}{3}(r_0 - r_i)^3 \right) \right]$$

where D_i and D_0 are the theoretical and strain-free

mineral-melt partition coefficients, respectively; r_0 is the optimum radius of the strain-free lattice site; r_i is the ionic radius of a given element; E is the effective Young's modulus; R is the gas constant (8·3145J/ mol·K); N_A is the Avogadro constant. The lattice strain parameters (D_0, r_0, E) are a function of pressure, temperature, melt and mineral composition, and they can be obtained by parameterization methods based on an extensive experimental dataset. Generalized parameterized schemes of REEs for clinopyroxene (Wood & Blundy, 1997), REEs for amphibole (Shimizu et al., 2017), and monovalent, divalent, and trivalent cations for plagioclase (Sun et al., 2017) were employed in this study. Predicted mineral-melt partition coefficients for samples in this study are shown in Fig. 15 using Onuma diagrams. These partition coefficients were then utilized to calculate the trace element concentrations in equilibrium melts.

Given the abundance of trace elements in crystals and available partitioning models, we focus our discussion on the equilibrium melt compositions that were calculated using REEs contents in clinopyroxene, REEs contents in amphibole, Sr and La contents in plagioclase. Equilibrium melt REE contents are shown in Fig. 16. The TME plagioclases give equilibrium melts with 531–868 ppm Sr. In contrast, the TQD plagioclase records equilibrium melts with 153–1229 ppm Sr. The

TQM plagioclases return equilibrium melts with 196– 853 ppm Sr. Due to the fact that clinopyroxene crystallization temperatures are similar to those of neighbouring plagioclases, they likely crystallized from the same melt. Thus, the comparison of calculated melt compositions in equilibrium with clinopyroxenes and neighbouring plagioclases can be used to assess the reliability of our calculated equilibrium melt compositions. The TME clinopyroxenes yield similar La contents in equilibrium melts (the average = $129 \pm 26\cdot7$ ppm of equilibrium melt La) to the TME plagioclase (the average = $133 \pm 28\cdot9$ ppm of equilibrium melt La), confirming the validity of our calculated equilibrium melt compositions. Whole-rock trace element compositions are commonly distinct from those of the calculated melts using clinopyroxene and plagioclase compositions. This discrepancy can be ascribed to either compaction-driven interstitial melt loss, or fractional loss of phases with high concentrations of trace elements, such as titanite and apatite, which minerals are found as inclusions in the principal minerals (Fig. 5g).

In combination with magmatic intensive variables, the overall suite of clinopyroxene, plagioclase and amphibole trace element data carry important information about the subtle variations in melt compositions within the plumbing system. Chondrite-normalized REE patterns of calculated equilibrium melts are shown in
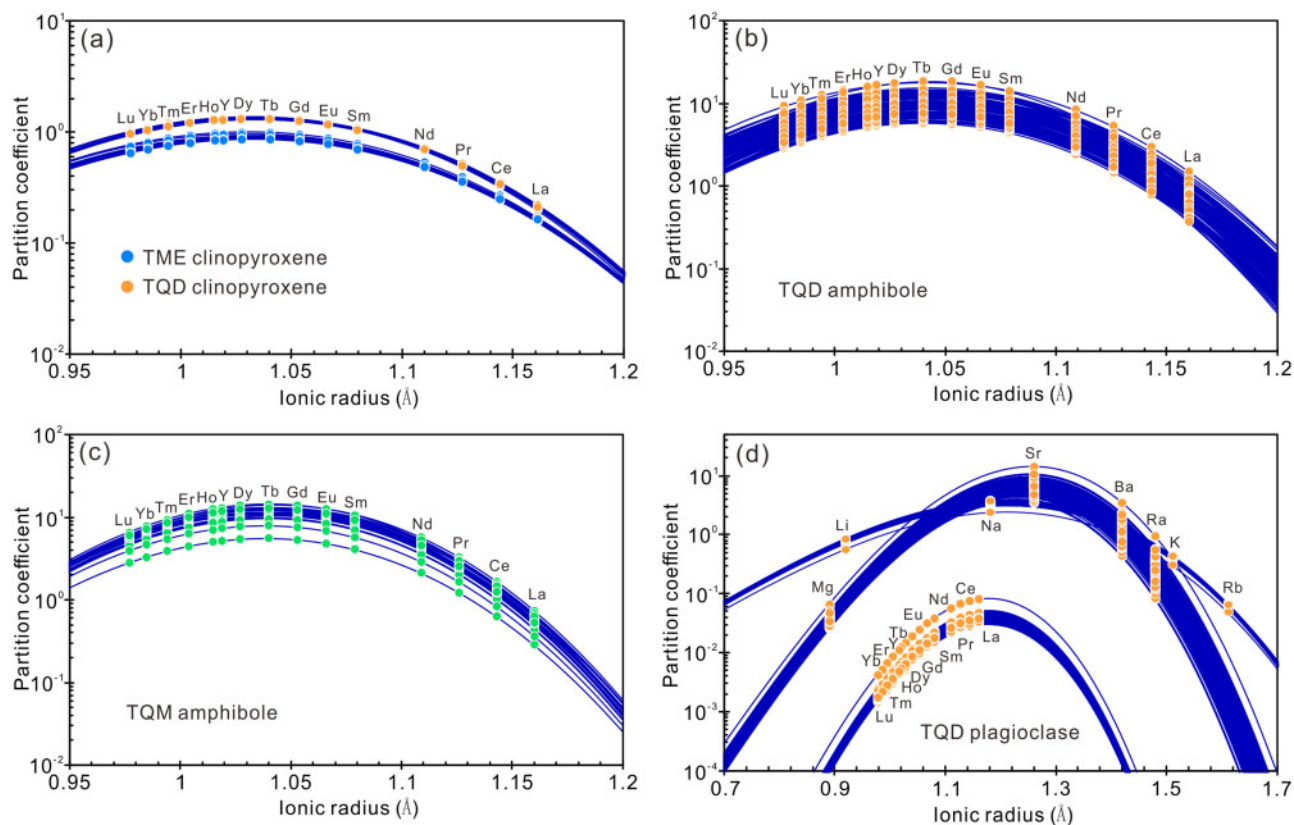

Fig. 15. Onuma diagrams for trace element partition coefficients as a function of cation radius. All partition coefficients and parabolas were predicted by the lattice strain model (Blundy & Wood, 1994). The lattice strain parameters (D_0, r_0, E) were obtained by generalized parameterized schemes that included REE for clinopyroxene (Wood & Blundy, 1997), REE for amphibole (Shimizu et al., 2017), and monovalent, divalent and trivalent cations for plagioclase (Sun et al., 2017) were employed in this study.

Fig. 16, and most of them have similar shapes. Systematic variations can also be identified that demonstrate the extent of HREE depletions increases with the evolution of magmas within the system (Fig. 16). Plagioclase is a ubiquitous phase in all igneous units (Figs 4 and 5), and so we might expect that evolved melts would be characterized by strong negative Eu anomalies. However, these are not observed in most equilibrium melts, which commonly display only moderate negative Eu anomalies (Figs 16 and 17a), even for high-silica melts as recorded by the amphiboles (Figs 11c, 16c, and d). This discrepancy can be ascribed to the fact that the TQD and TQM magmas have high f_{O2} (TQD: $\Delta NNO = 1\cdot4 \pm 0\cdot3$, TQM: $\Delta NNO = 1\cdot7 \pm 0\cdot3$; Fig. 11b; Table 1). Although Eu^{2+} can substitute for Ca^{2+} in plagioclase efficiently (e.g. Blundy & Wood, 1994), its abundance in oxidized melts is limited, leading to relatively low partition coefficient of Eu (Aigner-Torres et al., 2007). It is consistent with the low Eu contents in the TME, TQD and TQM plagioclases (Supplementary Table S3). Dy/Dy*, defined as Dy/(Dy*) = Dy_N/$(La_N^{(4/13)}*Yb_N^{(9/13)})$ (Davidson et al., 2013), was employed to track the variations in the curvature of REE patterns. As illustrated in Fig. 17b, Dy/Dy* decreases continuously with progressive magmatic evolution within the plumbing system. Clinopyroxene, amphibole and

titanite fractionation can generate significant modifications of REE content in residual melts (Davidson et al., 2013; Kohn, 2017). The primitive magmas in the Tieshan magmatic system were characterized by lower water contents (Fig. 13), so the precipitation of amphibole took place only after the development of H_2O-rich melts, consistent with lower crystallization temperatures (Fig. 11a) and highly evolved equilibrium melt compositions calculated for the TQD and TQM amphiboles (Fig. 11c). Thus, the decrease of Dy/Dy* ratios in the Tieshan plumbing system was likely driven by clinopyroxene and titanite fractionation (Fig. 5).

The parental magmas associated with magmatic-hydrothermal ore deposits from various tectonic settings commonly have high Sr/Y ratios, particularly for porphyry Cu deposits (e.g. Wang et al., 2004, 2006a, 2006b, 2014; Hou et al., 2009, 2015; Richards, 2011; Chiaradia et al., 2012; Lu et al., 2015; Yang et al., 2015; Zheng et al., 2019). In East China, several processes have been proposed for the genesis of high Sr/Y magmas, including (1) partial melting of subducted mid-ocean ridge or oceanic slab (e.g. Sun et al., 2007, 2011; Ling et al., 2009; Liu et al., 2010); (2) fractional crystallization of amphibole (e.g. Li et al., 2009, 2013); and (3) partial melting of delaminated lower crust (e.g. Wang et al., 2004, 2006a, 2006b, 2007; Xu et al., 2014; Zhu
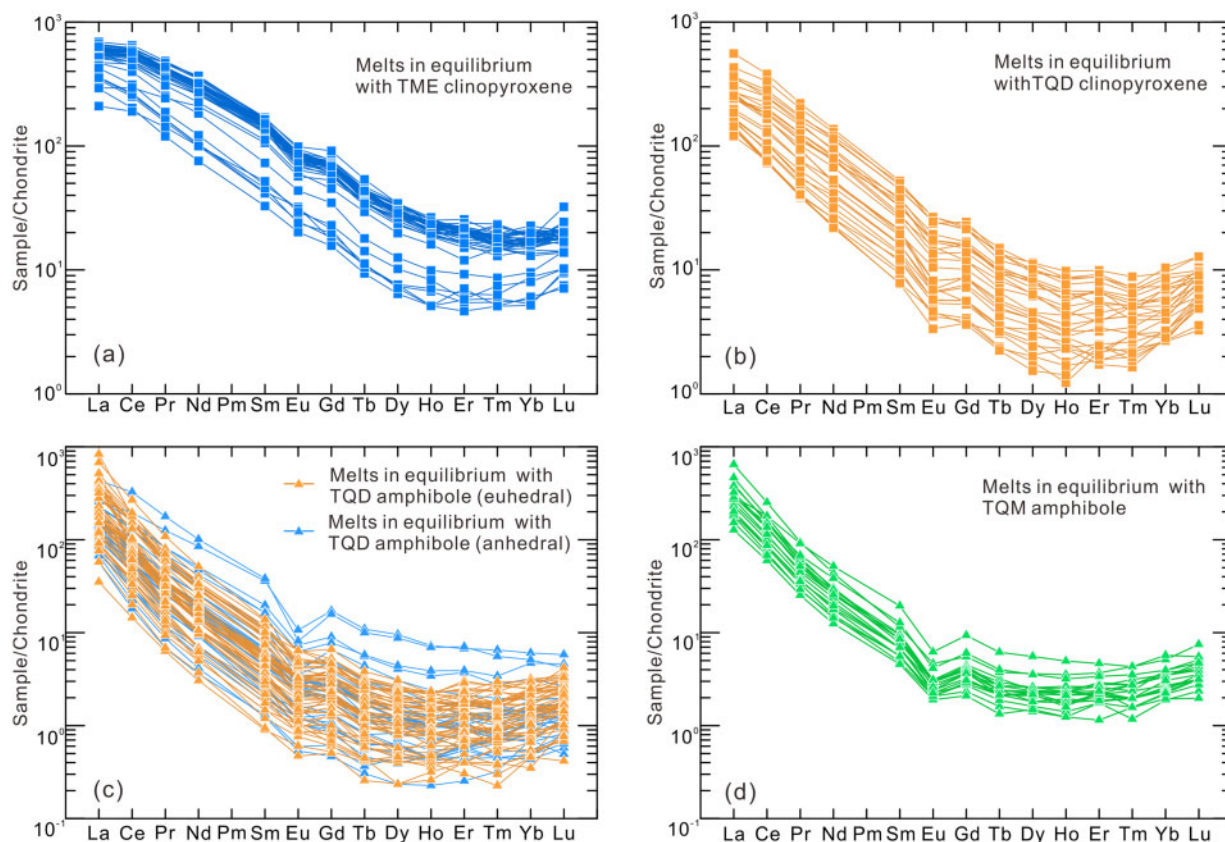

Fig. 16. Chondrite-normalized (Sun & McDonough 1989) rare earth element diagrams of the calculated melts in equilibrium with clinopyroxene and amphibole. (a) Melts in equilibrium with the clinopyroxenes from the Tieshan mafic enclaves. (b) Equilibrium melts for the clinopyroxenes from the Tieshan quartz diorite. (c) Melts in equilibrium with the amphiboles from the Tieshan quartz diorite. (d) Melts in equilibrium with the amphiboles from the Tonglushan quartz monzodiorite.
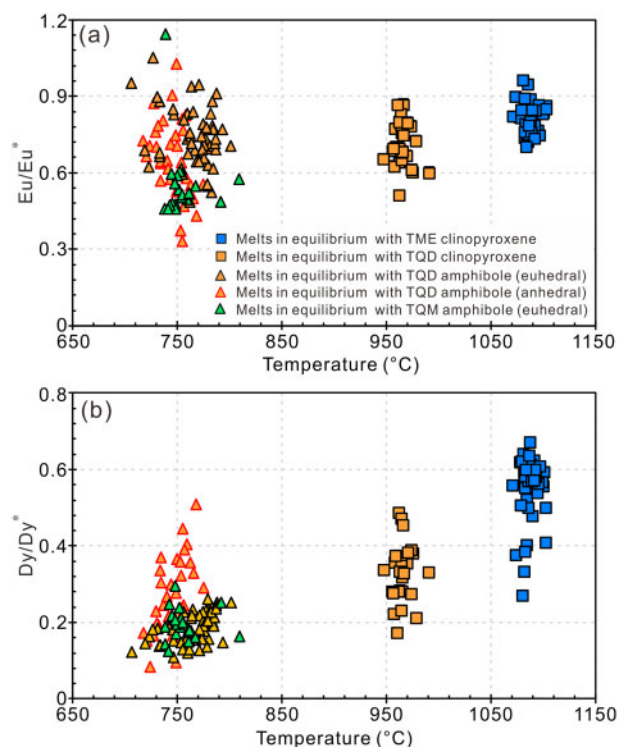
Fig. 17. (a) Plot of equilibrium melt Eu/Eu* as a function of temperatures. (b) Plot of equilibrium melt Dy/Dy* as a function of temperatures. Equilibrium melt compositions were calculated using our predicted partition coefficients by the lattice strain model. Temperatures were obtained by clinopyroxene–liquid thermobarometry (Neave & Putirka, 2017) and the amphibole thermometer (Putirka, 2016).

et al., 2014; Jia *et al.*, 2016). The most commonly invoked process for the interpretation of the association between porphyry systems and high Sr/Y magmas is hydrous crystal fractionation (e.g. Loucks, 2014), because the elevated magmatic H_2O contents can suppress the saturation of plagioclase and facilitate amphibole fractionation (e.g. Sisson & Grove, 1993; Zimmer *et al.*, 2010), leading to the enrichment of Sr and depletion of Y in derivative products. This scenario is persuasive for arc magmatic systems due to higher water contents in primitive melts (Plank *et al.*, 2013). However, within initially water-poor magmatic systems, the precipitation of plagioclase occurs at early stages and amphibole appears only at the latest stages during the magmatic differentiation (e.g. Zimmer *et al.*, 2010), which is in good agreement with the findings of this study (Figs 11 and 13). Ubiquitous plagioclase crystals (Figs 4 and 5), high Sr abundances (Supplementary Table S3) and the available partitioning model (Sun *et al.*, 2017) allow us to track the evolution of melt Sr contents within the Tieshan plumbing system. The results show that the TME plagioclases crystallized from melts with high Sr contents (the average = 658 ± 63·8 ppm). In contrast, the TQD plagioclases crystallized from melts with lower Sr contents (the average = 460 ± 285 ppm). Thus, it is unlikely that the high Sr/Y magmas of the Edong district were generated by

hydrous crystal fractionation. Therefore we infer that the high Sr/Y signatures of the TME and TQD were inherited from their magma sources, i.e. that garnet was a residual phase during partial melting (Wang *et al.*, 2004). Alternatively, garnet fractionation occurred at deeper levels, which has been observed in some porphyry deposit systems (e.g. Rottier *et al.*, 2020).

A deep crustal magma reservoir feeding the shallower magmatic-hydrothermal system

Our results for the reconstruction of the Tieshan magma plumbing system support a scenario where a shallow magmatic-hydrothermal system was supplied by a deep crustal magma reservoir. The fertility of magmas associated with ore deposits genesis was enhanced by increasing magmatic H_2O contents from 0·8–1·7 wt % to 2·1–2·8 wt % within the deep reservoir, followed by another increase in the shallow magma body (Fig. 18). Ore-forming magmas are not necessarily enriched in metals (e.g. Audétat, 2015; Chelle-Michou *et al.*, 2017), but there is a general agreement that fertile magmas must be H_2O-rich (>∼4 wt %; Sillitoe, 2010). Fluid saturation and subsequent exsolution of a magma chamber are the most critical steps in the formation of magmatic-hydrothermal ore deposits (Hedenquist & Lowenstern, 1994; Candela, 1997; Candela & Piccoli, 2005; Zajacz *et al.*, 2008; Audétat & Simon, 2012). Therefore, the transfer and evolution of magmas from the deep accumulation reservoir to shallow levels within a vertically extensive plumbing system appears to be an important process during the formation of magmatic-hydrothermal ore deposits, particularly for initially water-poor tectono-magmatic settings, which typically have primitive H_2O contents of <1·5 wt % (Wallace *et al.*, 2015). A similar key role of deep crustal magma chambers in the formation of porphyry deposits has also been recognized in subduction (Chiaradia & Caricchi, 2017) and post-subduction settings (Rottier *et al.*, 2020). We thus propose that feeding of shallow magmatic-hydrothermal systems by deep crustal magma reservoirs is not limited to initially water-poor environments, but is also important in productive arc magmatic systems. However, the deposit sizes in the Edong district are orders of magnitude lower than the porphyry Cu deposits in typical subduction zones such as the Andes and Southwest Pacific regions (Seedorff *et al.*, 2005; Sillitoe, 2010). This means that initially water-poor systems can principally produce magmatic-hydrothermal ore deposits, but the size of these deposit is limited, consistent with modelling results showing that the formation of giant porphyry Cu deposits requires large volumes of magma and water (Chiaradia, 2020). In addition, magmatism associated with a deposit is usually active over a timescale of several millions of years (e.g. Chambefort *et al.*, 2008, 2013; Longo *et al.*, 2010; Chelle-Michou *et al.*, 2014). In contrast, hydrothermal activities often occur during the waning stages of their magmatic systems (Sillitoe, 2010;
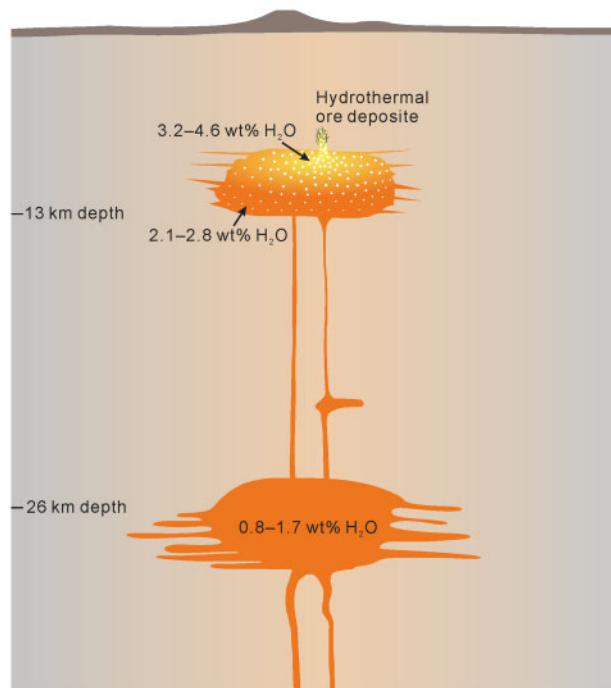
Fig. 18. Conceptual model of the Tieshan transcrustal magmatic system. A deep magma reservoir with a water content of 0·8–1·7 wt % fed the growth of the shallow magma chamber with an initial water content of 2·1–2·8 wt %. After extensive cooling-related crystallization, the shallow magma body turned relatively H_2O-rich with water contents ranging from 3·2 to 4·6 wt %, ultimately leading to magmas that were fertile for mineralization.

Audétat & Simon, 2012) and have much shorter time-scales (e.g. Chelle-Michou *et al.*, 2015; Buret *et al.*, 2016; Li *et al.*, 2017). The different durations of magmatic and hydrothermal processes within a deposit are likely to be reconciled by a scenario where a long-lived deep magma reservoir sustains the incremental growth of shallow magma chambers and extensive fluid exsolution occurs after the mature stage of a magma chamber is reached, consistent with the modeling results of Chiaradia & Caricchi (2017).

CONCLUSIONS

We have reconstructed the magma plumbing system beneath the Tieshan deposit, which may be typical of deposit formed in initially water-poor magmas. The textural and geochemical characteristics of various magmatic units, particularly their feature of bimodal crystallization pressures, record a wealth of information about the chemical and physical processes occurring in the system. Our results indicate that an intermediate magma reservoir in the deep crust fed the Tieshan magmatic-hydrothermal system. Two magmatic water enrichment processes have been recognized, including the separation and transfer of evolved melts from the deep magma reservoir to shallow levels and the continuous solidification of the shallow magma body. The former process enriched magmatic H_2O contents from

0·8–1·7 wt % to 2·1–2·8 wt %, and the latter process increased water contents in residual melts up to 3·2–4·6 wt %, ultimately leading to magmas becoming fertile for mineralization. Mineral trace element systematics provide further insights into the chemical evolution of the plumbing system. The deep crustal magma reservoir has higher Sr contents (the average $=$ 658 ± 64 ppm), suggesting that high Sr/Y magmatic signatures within initially water-poor systems were derived from their magma sources (i.e. garnet was a residual phase during partial melting) or garnet fractionation at more deep levels. Our results reveal that the deep crustal magma reservoir plays a critical role in the formation of shallow magmatic-hydrothermal systems. Not only does it lead to the enrichment of ore-forming materials such as water, the presence of a deep magma reservoir also sustains the incremental growth of shallow magma chambers.

SUPPLEMENTARY DATA

Supplementary data are available at *Journal of Petrology* online

REFERENCES

Aigner-Torres, M., Blundy, J. D., Ulmer, P. & Pettke, T. (2007). Laser Ablation ICPMS study of trace element partitioning between plagioclase and basaltic melts: an experimental approach. *Contributions to Mineralogy and Petrology* **153**, 647–667.

Arndt, N. T., Fontboté, L., Hedenquist, J. W., Kesler, S. E., Thompson, J. F. & Wood, D. G. (2017). Future global mineral resources. *Geochemical Perspectives* **6**, 1–171.

Audétat, A. (2015). Compositional evolution and formation conditions of magmas and fluids related to porphyry Mo mineralization at Climax, Colorado. *Journal of Petrology* **56**, 1519–1546.

Audétat, A. (2019). The metal content of magmatic-hydrothermal fluids and its relationship to mineralization potential. *Economic Geology* **114**, 1033–1056.

Audétat, A. & Li, W. (2017). The genesis of climax-type porphyry mo deposits: insights from fluid inclusions and melt inclusions. *Ore Geology Reviews* **88**, 436–450.

Audétat, A. & Simon, A. C. (2012). Magmatic controls on porphyry copper genesis. In: Hedenquist, J. W., Harris, M. & Camus, F. (eds) *Geology and Genesis of Major Copper Deposits and Districts of the world: A Tribute to Richard H. Sillitoe. Society of Economic Geologists, Special Publication* **16**, 553–572.

Bachmann, O. & Bergantz, G. W. (2004). On the origin of crystal-poor rhyolites: extracted from batholithic crystal mushes. *Journal of Petrology* **45**, 1565–1582.

Bachmann, O. & Huber, C. (2019). The inner workings of crustal distillation columns; the physical mechanisms and rates controlling phase separation in silicic magma reservoirs. *Journal of Petrology* **60**, 3–18.

Barnes, C. G., Memeti, V. & Coint, N. (2016). Deciphering magmatic processes in calc-alkaline plutons using trace element zoning in hornblende. *American Mineralogist* **101**, 328–342.

Barnes, C. G., Werts, K., Memeti, V. & Ardill, K. (2019). Most Granitoid Rocks are Cumulates: Deductions from Hornblende Compositions and Zircon Saturation. Journal of Petrology **60**, 2227–2240.10.1093/petrology/egaa008

Blundy, J. & Wood, B. (1994). Prediction of crystal–melt partition coefficients from elastic moduli. *Nature* **372**, 452–454.

Boudreau, A. (2016). Bubble migration in a compacting crystal-liquid mush. *Contributions to Mineralogy and Petrology* **171**, 32.

Buret, Y., von Quadt, A., Heinrich, C., Selby, D., Wälle, M. & Peytcheva, I. (2016). From a long-lived upper-crustal magma chamber to rapid porphyry copper emplacement: Reading the geochemistry of zircon crystals at Bajo de la Alumbrera (NW Argentina). *Earth and Planetary Science Letters* **450**, 120–131.

Candela, P. A. (1997). A review of shallow, ore-related granites: textures, volatiles, and ore metals. *Journal of Petrology* **38**, 1619–1633.

Candela, P. A. & Piccoli, P. M. (2005). Magmatic processes in the development of porphyry-type ore systems. In: Hedenquist, J. W., Thompson, J. F. H., Goldfarb, R. J. & Richards, J. P. (eds) *Economic Geology 100th Anniversary Volume: Society of Economic Geologists*. Littleton, Colorado, pp. 25–37.

Carten, R. B., White, W. H. & Stein, H. J. (1993). High-grade granite-related molybdenum systems: Classification and origin. In: Kirkham, R. V., Sinclair, W. D., Thorpe, R. I. & Duke, J. M. (eds) Mineral Deposit Modeling. *Geological Association of Canada, Special Paper* **40**, 521–554.

Cathles, L. M. & Shannon, R. (2007). How potassium silicate alteration suggests the formation of porphyry ore deposits begins with the nearly explosive but barren expulsion of large volumes of magmatic water. *Earth and Planetary Science Letters* **262**, 92–108.

Chambefort, I., Dilles, J. H. & Kent, A. J. (2008). Anhydrite-bearing andesite and dacite as a source for sulfur in magmatic-hydrothermal mineral deposits. *Geology* **36**, 719–722.

Chambefort, I., Dilles, J. H. & Longo, A. A. (2013). Amphibole geochemistry of the Yanacocha Volcanics, Peru: Evidence for diverse sources of magmatic volatiles related to gold ores. *Journal of Petrology* **54**, 1017–1046.

Chang, Y. F., Liu, X. P. & Wu, C. Y. (1991). *The Copper–Iron Belt of the Lower and Middle Reaches of the Changjiang River*. Beijing: Geological Publishing House, p. 234 (in Chinese).

Chelle-Michou, C., Chiaradia, M., Ovtcharova, M., Ulianov, A. & Wotzlaw, J. F. (2014). Zircon petrochronology reveals the temporal link between porphyry systems and the magmatic evolution of their hidden plutonic roots (the Eocene Coroccohuayco deposit, Peru). *Lithos* **198-199**, 129–140.

Chelle-Michou, C., Chiaradia, M., Selby, D., Ovtcharova, M. & Spikings, R. A. (2015). High-resolution geochronology of the Coroccohuayco porphyry-skarn deposit, Peru: a rapid product of the Incaic Orogeny. *Economic Geology* **110**, 423–443.

Chelle-Michou, C., Rottier, B., Caricchi, L. & Simpson, G. (2017). Tempo of magma degassing and the genesis of porphyry copper deposits. *Scientific Reports* **7**, 40566.

Chiaradia, M. (2020). Gold endowments of porphyry deposits controlled by precipitation efficiency. *Nature Communications* **11**, 248.

Chiaradia, M. & Caricchi, L. (2017). Stochastic modelling of deep magmatic controls on porphyry copper deposit endowment. *Scientific Reports* **7**, 44523.

Chiaradia, M., Ulianov, A., Kouzmanov, K. & Beate, B. (2012). Why large porphyry Cu deposits like high Sr/Y magmas? *Scientific Reports* **2**, 685.

Cline, J. S. & Bodnar, R. J. (1991). Can economic porphyry copper mineralization be generated by a typical calc-alkaline melt? *Journal of Geophysical Research* **96**, 8113–8126.

Costa, F., Chakraborty, S. & Dohmen, R. (2003). Diffusion coupling between trace and major elements and a model for calculation of magma residence times using plagioclase. *Geochimica et Cosmochimica Acta* **67**, 2189–2200.

Davidson, J., Turner, S. & Plank, T. (2013). Dy/Dy*: variations arising from mantle sources and petrogenetic processes. *Journal of Petrology* **54**, 525–537.

Duan, D. & Jiang, S. (2017). In situ major and trace element analysis of amphiboles in quartz monzodiorite porphyry from the Tonglvshan Cu–Fe (Au) deposit, Hubei Province, China: insights into magma evolution and related mineralization. *Contributions to Mineralogy and Petrology* **172**, 36.

Ducea, M. N., Saleeby, J. B. & Bergantz, G. (2015). The architecture, chemistry, and evolution of continental magmatic arcs. *Annual Review of Earth and Planetary Sciences* **43**, 299–331.

Erdmann, S., Martel, C., Pichavant, M. & Kushnir, A. (2014). Amphibole as an archivist of magmatic crystallization conditions: problems, potential, and implications for inferring magma storage prior to the paroxysmal 2010 eruption of *Mount Merapi*, Indonesia. *Contributions to Mineralogy and Petrology* **167**, 1016.

Gao, S., Rudnick, R. L., Yuan, H., Liu, X., Liu, Y., Xu, W., Ling, W., Ayers, J., Wang, X. & Wang, Q. (2004). Recycling lower continental crust in the North China craton. *Nature* **432**, 892–897.

Grove, T., Parman, S., Bowring, S., Price, R. & Baker, M. (2002). The role of an H_2O-rich fluid component in the generation of primitive basaltic andesites and andesites from the Mt. Shasta region, N California. *Contributions to Mineralogy and Petrology* **142**, 375–396.

Hawkesworth, C. J., Gallagher, K., Hergt, J. M. & McDermott, F. (1993). Mantle and slab contributions in arc magmas. *Annual Review of Earth and Planetary Sciences* **21**, 175–204.

Hedenquist, J. W. & Lowenstern, J. B. (1994). The role of magmas in the formation of hydrothermal ore deposits. *Nature* **370**, 519–527.

Hou, Z., Yang, Z., Qu, X., Meng, X., Li, Z., Beaudoin, G., Rui, Z., Gao, Y. & Zaw, K. (2009). The Miocene Gangdese porphyry copper belt generated during post-collisional extension in the Tibetan Orogen. *Ore Geology Reviews* **36**, 25–51.

Hou, Z. Q., Duan, L. F., Lu, Y. J., Zheng, Y. C., Zhu, D. C., Yang, Z. M., Yang, Z. S., Wang, B. D., Pei, Y. R., Zhao, Z. D. & McCuaig, C. (2015). Lithospheric architecture of the Lhasa

terrane and its control on ore deposits in the Himalayan-Tibetan orogen. *Economic Geology* **110**, 1541–1575.

Hou, Z. Q., Pan, X. F., Li, Q. Y., Yang, Z. M. & Song, Y. C. (2013). The giant Dexing porphyry CuMo-Au deposit in east China, product of melting of juvenile lower crust in an intracontinental setting. *Mineralium Deposita* **48**, 1019–1045.

Jerram, D. A. & Martin, V. M. (2008). Understanding crystal populations and their significance through the magma plumbing system. In: Annen, C. & Zellmer, G. F. (eds) Dynamics of Crustal Magma Transfer, Storage and Differentiation. *Geological Society, London, Special Publications* **304**, 133–148.

Jia, L. Q., Mo, X. X., Santosh, M., Yang, Z. S., Yang, D., Dong, G. C., Wang, L., Wang, X. C. & Wu, X. (2016). Early cretaceous continental delamination in the Yangtze Block: evidence from high-Mg adakitic intrusions along the Tanlu fault, central Eastern China. *Journal of Asian Earth Sciences* **127**, 152–169.

Kohn, M. J. (2017). Titanite petrochronology. *Reviews in Mineralogy and Geochemistry* **83**, 419–441.

Leake, B. E., Woolet, A. R., Arps, C. E. S., Birch, W. D., Gilbert, M. C., Grice, J. D., Hawthorne, F. C., Kato, A., Kisch, H. J. & Krivovichev, E. A. (1997). Nomenclature of amphiboles: report of the subcommittee on amphiboles of the International Mineralogical Association, Commission on New Minerals and Mineral Names. *The Canadian Mineralogist* **35**, 219–246.

Li, J. W., Vasconcelos, P. M., Zhou, M. F., Deng, X. D., Cohen, B., Bi, S. J., Zhao, X. F. & Selby, D. (2014). Longevity of magmatic-hydrothermal systems in the Daye Cu-Fe-Au district, eastern China with implications for mineral exploration. *Ore Geology Reviews* **57**, 375–392.

Li, J. W., Zhao, X. F., Zhou, M. F., Ma, C. Q., de Souza, Z. S. & Vasconcelos, P. (2009). Late Mesozoic magmatism from the Daye region, eastern China: U–Pb ages, petrogenesis, and geodynamic implications. *Contributions to Mineralogy and Petrology* **157**, 383–409.

Li, J. W., Zhao, X. F., Zhou, M. F., Vasconcelos, P., Ma, C. Q., Deng, X. D., de Souza, Z. S., Zhao, Y. X. & Wu, G. (2008). Origin of the Tongshankou porphyry-skarn Cu–Mo deposit, eastern Yangtze craton, Eastern China: eochronological, geochemical, and Sr–Nd–Hf isotopic constraints. *Mineralium Deposita* **43**, 315–336.

Li, W., Xie, G., Mao, J., Zhu, Q. & Zheng, J. (2019). Mineralogy, fluid inclusion, and stable isotope studies of the Chengchao deposit, Hubei Province, Eastern China. *Economic Geology* **114**, 325–352.

Li, X. H., Li, Z. X., Li, W. X., Wang, X. C. & Gao, Y. (2013). Revisiting the "C-type adakites" of the Lower Yangtze River Belt, central eastern China: in-situ zircon Hf–O isotope and geochemical constraints. *Chemical Geology* **345**, 1–15.

Li, X. H., Li, Z. X., Zhou, H. W., Liu, Y. & Kinny, P. D. (2002). U-Pb zircon geochronology, geochemistry and Nd isotopic study of Neoprozoic bimodal volcanic rocks in the Kangdian Rift of south China: implications for the initial rifting of Rodinia. *Precambrian Research* **113**, 135–154.

Li, Y., Selby, D., Condon, D. & Tapster, S. (2017). Cyclic magmatic-hydrothermal evolution in porphyry systems: high-precision U-Pb and Re-Os geochronology constraints on the Tibetan Qulong porphyry Cu-Mo deposit. *Economic Geology* **112**, 1419–1440.

Li, Z. X. & Li, X. H. (2007). Formation of the 1300-km-wide intracontinental orogen and postorogenic magmatic province in Mesozoic South China: a flat-slab subduction model. *Geology* **35**, 179–182.

Ling, M. X., Wang, F. Y., Ding, X., Hu, Y. H., Zhou, J. B., Zartman, R. E., Yang, X. Y. & Sun, W. (2009). Cretaceous ridge subduction along the lower Yangtze River belt, eastern China. *Economic Geology* **104**, 303–321.

Liu, S. A., Li, S., He, Y. & Huang, F. (2010). Geochemical contrasts between early Cretaceous ore-bearing and ore-barren high-Mg adakites in central-eastern China: implications for petrogenesis and Cu–Au mineralization. *Geochimica et Cosmochimica Acta* **74**, 7160–7178.

Longo, A. A., Dilles, J. H., Grunder, A. L. & Duncan, R. (2010). Evolution of calc-alkaline volcanism and associated hydrothermal gold deposits at Yanacocha, Peru. *Economic Geology* **105**, 1191–1241.

Loucks, R. R. (2014). Distinctive composition of copper-ore-forming arc magmas. *Australian Journal of Earth Sciences* **61**, 5–16.

Lu, Y. J., Loucks, R. R., Fiorentini, M. L., Yang, Z. M. & Hou, Z. Q. (2015). Fluid flux melting generated postcollisional high Sr/Y copper ore-forming water-rich magmas in Tibet. *Geology* **43**, 583–586.

Ludington, S. & Plumlee, G. S. (2009). Climax-type porphyry molybdenum deposits. US Geological Survey, Open-File Report 2009–1215, p. 16.

Mao, J., Xie, G., Duan, C., Pirajno, F., Ishiyama, D. & Chen, Y. (2011). A tectono-genetic model for porphyry–skarn–stratabound Cu–Au–Mo–Fe and magnetite–apatite deposits along the Middle–Lower Yangtze River Valley, Eastern China. *Ore Geology Reviews* **43**, 294–314.

Meinert, L. D., Dipple, G. M. & Nicolescu, S. (2005). World skarn deposits. *Economic Geology 100th Anniversary* **29**, 299–336.

Morimoto, N. (1988). Nomenclature of pyroxenes. *Mineralogy and Petrology* **39**, 55–76.

Neave, D. A. & Putirka, K. D. (2017). A new clinopyroxene-liquid barometer, and implications for magma storage pressures under Icelandic rift zones. *American Mineralogist* **102**, 777–794.

O'Neill, H. S. C. & Pownceby, M. I. (1993). Thermodynamic data from redox reactions at high temperatures. I. An experimental and theoretical assessment of the electrochemical method using stabilized zirconia electrolytes, with revised values for the Fe-"FeO", Co-CoO, Ni-NiO and Cu-Cu_2O oxygen buffers, and new data for the W-WO_2 buffer. *Contributions to Mineralogy and Petrology* **114**, 296–314.

Pirajno, F. & Zhou, T. (2015). Intracontinental porphyry and porphyry-skarn mineral systems in eastern china: scrutiny of a special case "made-in-China. *Economic Geology* **110**, 603–629.

Plank, T., Kelley, K. A., Zimmer, M. M., Hauri, E. H. & Wallace, P. J. (2013). Why do mafic arc magmas contain~ 4 wt % water on average? *Earth and Planetary Science Letters* **364**, 168–179.

Portnyagin, M., Almeev, R., Matveev, S. & Holtz, F. (2008). Experimental evidence for rapid water exchange between melt inclusions in olivine and host magma. *Earth and Planetary Science Letters* **272**, 541–552.

Putirka, K. (2016). Amphibole thermometers and barometers for igneous systems and some implications for eruption mechanisms of felsic magmas at arc volcanoes. *American Mineralogist* **101**, 841–858.

Putirka, K. D. (2008). Thermometers and barometers for volcanic systems. *Reviews in Mineralogy and Geochemistry* **69**, 61–120.

Putirka, K. D., Canchola, J., Rash, J., Smith, O., Torrez, G., Paterson, S. R. & Ducea, M. N. (2014). Pluton assembly and the genesis of granitic magmas: insights from the GIC

pluton in cross section, Sierra Nevada Batholith, California. *American Mineralogist* **99**, 1284–1303.

Richards, J. P. (2003). Tectono-magmatic precursors for porphyry Cu-(Mo-Au) deposit formation. *Economic Geology* **98**, 1515–1533.

Richards, J. P. (2011). High Sr/Y arc magmas and porphyry Cu±Mo±Au deposits: just add water. *Economic Geology* **106**, 1075–1081.

Ridolfi, F., Renzulli, A. & Puerini, M. (2010). Stability and chemical equilibrium of amphibole in calc-alkaline magmas: an overview, new thermobarometric formulations and application to subduction-related volcanoes. *Contributions to Mineralogy and Petrology* **160**, 45–66.

Rottier, B., Audétat, A., Koděra, P. & Lexa, J. (2020). Origin and evolution of magmas in the porphyry Au-mineralized Javorie volcano (Central Slovakia): evidence from thermobarometry, melt inclusions, and sulfide inclusions. *Journal of Petrology* in press. doi: 10.1093/petrology/egaa014.

Rottier, B., Rezeau, H., Casanova, V., Kouzmanov, K., Moritz, R., Schlöglova, K., Wälle, M. & Fontboté, L. (2017). Trace element diffusion and incorporation in quartz during heating experiments. *Contributions to Mineralogy and Petrology* **172**, 23.

Seedorff, E., Dilles, J. H., Proffett, J. M., Einaudi, M. T., Zurcher, L., Stavast, W. J. A., Johnson, D. A. & Barton, M. D. (2005). Porphyry deposits: characteristics and origin of hypogene features. *Economic Geology 100th Anniversary* **29**, 251–298.

Shimizu, K., Liang, Y., Sun, C., Jackson, C. R. & Saal, A. E. (2017). Parameterized lattice strain models for REE partitioning between amphibole and silicate melt. *American Mineralogist* **102**, 2254–2267.

Sillitoe, R. H. (2010). Porphyry copper systems. *Economic Geology* **105**, 3–41.

Sillitoe, R. H. (2018). Why no porphyry copper deposits in Japan and South Korea? *Resource Geology* **68**, 107–125.

Simon, A. C. & Ripley, E. M. (2011). The role of magmatic sulfur in the formation of ore deposits. *Reviews in Mineralogy and Geochemistry* **73**, 513–578.

Sisson, T. W. & Grove, T. L. (1993). Experimental investigations of the role of H_2O in calc-alkaline differentiation and subduction zone magmatism. *Contributions to Mineralogy and Petrology* **113**, 143–166.

Sun, C., Graff, M. & Liang, Y. (2017). Trace element partitioning between plagioclase and silicate melt: the importance of temperature and plagioclase composition, with implications for terrestrial and lunar magmatism. *Geochimica et Cosmochimica Acta* **206**, 273–295.

Sun, S. S. & McDonough, W. F. (1989). Chemical and isotopic systematics of oceanic basalts: implication for mantle composition and processes. In: Saunder, A. D. & Norry, M. J. (eds), Magmatism in the Ocean Basins. *Geological Society Special Publication* **42**, 313–345.

Sun, W., Ding, X., Hu, Y. H. & Li, X. H. (2007). The golden transformation of the cretaceous plate subduction in the west pacific. *Earth and Planetary Science Letters* **262**, 533–542.

Sun, W., Zhang, H., Ling, M.-X., Ding, X., Chung, S.-L., Zhou, J., Yang, X.-Y. & Fan, W. (2011). The genetic association of adakites and Cu–Au ore deposits. *International Geology Review* **53**, 691–703.

Tatsumi, Y. (1989). Migration of fluid phases and genesis of basalt magmas in subduction zones. *Journal of Geophysical Research: Solid Earth* **94**, 4697–4707.

Ulmer, P. & Trommsdorff, V. (1995). Serpentine stability to mantle depths and subduction-related magmatism. *Science* **268**, 858–861.

Vernon, R. H. (2004). *A Practical Guide to Rock Microstructure*. Cambridge: Cambridge University Press.

Wallace, P. J., Plank, T., Edmonds, M. & Hauri, E. H. (2015). Volatiles in magmas. In: Sigurdsson, H. (ed.) *The Encyclopedia of Volcanoes*, 2nd edn. Amsterdam: Academic Press, pp. 163–183.

Wang, F., Liu, S. A., Li, S. & He, Y. (2013). Contrasting zircon Hf–O isotopes and trace elements between ore-bearing and ore-barren adakitic rocks in central-eastern China: implications for genetic relation to Cu–Au mineralization. *Lithos* **156-159**, 97–111.

Wang, Q., Xu, J. F., Jian, P., Bao, Z. W., Zhao, Z. H., Li, C. F., Xiong, X. L. & Ma, J. L. (2006a). Petrogenesis of adakitic porphyries in an extensional tectonic setting, Dexing, South China: implications for the genesis of porphyry copper mineralization. *Journal of Petrology* **47**, 119–144.

Wang, Q., Wyman, A., Xu, J. F., Jian, P., Zhao, Z. H., Li, C. F., Xu, W., Ma, J. L. & He, B. (2007). Early Cretaceous adakitic granites in the Northern Dabie complex, central China: implications for partial melting and delamination of thickened lower crust. *Geochimica et Cosmochimica Acta* **71**, 2609–2636.

Wang, Q., Wyman, D. A., Xu, J. F., Zhao, Z. H., Jian, P., Xiong, X. L., Bao, Z. W., Li, C. F. & Bai, Z. H. (2006b). Petrogenesis of Cretaceous adakitic and shoshonitic igneous rocks in the Luzong area, Anhui Province (eastern China): Implications for geodynamics and Cu-Au mineralization. *Lithos* **89**, 424–446.

Wang, Q., Zhao, Z. H., Bao, Z. W., Xu, J. F., Liu, W., Li, C. F., Bai, Z. H. & Xiong, X. L. (2004). Geochemistry and petrogenesis of the Tongshankou and Yinzu adakitic intrusive rocks and the associated porphyry copper-molybdenum mineralization in southeast Hubei, east China. *Resource Geology* **54**, 137–152.

Wang, R., Richards, J. P., Hou, Z., Yang, Z. & DuFrane, S. A. (2014). Increased magmatic water content—the key to Oligo-Miocene porphyry Cu-Mo±Au formation in the eastern Gangdese belt. *Economic Geology* **109**, 1315–1339.

Waters, L. E. & Lange, R. A. (2015). An updated calibration of the plagioclase-liquid hygrometer-thermometer applicable to basalts through rhyolites. *American Mineralogist* **100**, 2172–2184.

Wiebe, R. A., Manon, M. R., Hawkins, D. P. & McDonough, W. F. (2004). Late-stage mafic injection and thermal rejuvenation of the Vinalhaven granite, coastal Maine. *Journal of Petrology* **45**, 2133–2153.

Wood, B. J. & Blundy, J. D. (1997). A predictive model for rare earth element partitioning between clinopyroxene and anhydrous silicate melt. *Contributions to Mineralogy and Petrology* **129**, 166–181.

Wörner, G., Mamani, M. & Blum-Oeste, M. (2018). Magmatism in the Central Andes. *Elements* **14**, 237–244.

Xie, G., Mao, J., Xiongwei, L., Duan, C. & Yao, L. (2011a). Late Mesozoic bimodal volcanic rocks in the Jinniu basin, Middle–Lower Yangtze River Belt (YRB). *Lithos* **127**, 144–164.

Xie, G., Mao, J. & Zhao, H. (2011b). Zircon U–Pb geochronological and Hf isotopic constraints on petrogenesis of Late Mesozoic intrusions in the southeast Hubei Province, Middle–Lower Yangtze River belt (MLYRB), East China. *Lithos* **125**, 693–710.

Xie, G.Q., Mao, J.W., Li, R.L., Qu, W.J., Pirajno, F. and Du, A.D. (2007). ReOs molybdenite and ArAr phlogopite dating of CuFeAuMo (W) deposits in southeastern Hubei, China. *Mineralogy and Petrology* **90**, 249–270.

Xu, J. F., Shinjo, R., Defant, M. J., Wang, Q. & Rapp, R. P. (2002). Origin of Mesozoic adakitic intrusive rocks in the Ningzhen area of east China: partial melting of delaminated lower continental crust? *Geology* **30**, 1111–1114.

Xu, Y. M., Jiang, S. Y., Zhu, Z. Y., Yang, S. Y. & Zhou, W. (2014). Petrogenesis of Late Mesozoic granitoids and coeval mafic rocks from the Jiurui district in the Middle–Lower Yangtze metallogenic belt of Eastern China: Geochemical and Sr–Nd–Pb–Hf isotopic evidence. *Lithos* **190–191**, 467–484.

Yang, Z. M., Lu, Y. J., Hou, Z. Q. & Chang, Z. S. (2015). High-Mg diorite from Qulong in southern Tibet: implications for the genesis of adakite-like intrusions and associated porphyry Cu deposits in collisional orogens. *Journal of Petrology* **56**, 227–254.

Zajacz, Z., Halter, W. E., Pettke, T. & Guillong, M. (2008). Determination of fluid/melt partition coefficients by LA-ICPMS analysis of co-existing fluid and silicate melt inclusions: controls on element partitioning. *Geochimica et Cosmochimica Acta* **72**, 2169–2197.

Zellmer, G. F., Edmonds, M. & Straub, S. M. (2015). Volatiles in subduction zone magmatism. *Geological Society, London, Special Publications* **410**, 1–17.

Zellmer, G. F., Iizuka, Y., Miyoshi, M., Tamura, Y. & Tatsumi, Y. (2012). Lower crustal H_2O controls on the formation of adakitic melts. *Geology* **40**, 487–490.

Zhang, H.-F., Sun, M., Zhou, X.-H., Fan, W.-M., Zhai, M.-G. & Yin, J.-F. (2002). Mesozoic lithosphere destruction beneath the North China Craton: evidence from major- and trace-elements and Sr–Nd–Pb isotope studies of Fangcheng basalts. *Contributions to Mineralogy and Petrology* **144**, 241–253.

Zhang, L., Ren, Z. Y., Xia, X. P., Yang, Q., Hong, L. B. & Wu, D. (2019). In situ determination of trace elements in melt inclusions using laser ablation inductively coupled plasma sector field mass spectrometry. *Rapid Communications in Mass Spectrometry* **33**, 361–370.

Zheng, Y. C., Liu, S. A., Wu, C. D., Griffin, W. L., Li, Z. Q., Xu, B., Yang, Z. M., Hou, Z. Q. & O'Reilly, S. Y. (2019). Cu isotopes reveal initial Cu enrichment in sources of giant porphyry deposits in a collisional setting. *Geology* **47**, 135–138.

Zhou, J.-S., Yang, Z.-S., Hou, Z.-Q. & Wang, Q. (2020a). Amphibole-rich cumulate xenoliths in the Zhazhalong intrusive suite, Gangdese arc: implications for the role of amphibole fractionation during magma evolution. *American Mineralogist* **105**, 262–275.

Zhou, J.-S., Yang, Z.-S., Wang, Q., Zheng, Y.-C., Hou, Z.-Q. & Wyman, D. A. (2020b). Extraction of high-silica granites from an upper crustal magma reservoir: insights from the Narusongduo magmatic system, Gangdese arc. *American Mineralogist, in Press* doi: 10.2138/am-2020-7369.

Zhou, T., Wang, S., Fan, Y., Yuan, F., Zhang, D. & White, N. C. (2015). A review of the intracontinental porphyry deposits in the Middle-Lower Yangtze River Valley metallogenic belt, Eastern China. *Ore Geology Reviews* **65**, 433–456.

Zhou, X. M. & Li, W. X. (2000). Origin of late mesozoic igneous rocks in southeastern china: implications for lithosphere subduction and underplating of mafic magmas. *Tectonophysics* **326**, 269–287.

Zhu, Q. Q., Xie, G. Q. & Li, W. (2019). Superposition mechanism of Fe enrichment in skarn deposits of Edong district: constrains from magnetite texture and ore grade data. *Acta Petrologica Sinica* **35**, 3703–3720 (in Chinese with English abstract).

Zhu, Z. Y., Jiang, S. Y., Hu, J., Gu, L. X. & Li, J. (2014). Geochronology, geochemistry, and mineralization of the granodiorite porphyry hosting the Matou Cu–Mo ($\pm$W) deposit, Lower Yangtze River metallogenic belt, eastern. *Journal of Asian Earth Sciences* **79**, 623–640.

Zimmer, M. M., Plank, T., Hauri, E. H., Yogodzinski, G. M., Stelling, P., Larsen, J., Singer, B., Jicha, B., Mandeville, C. & Nye, C. J. (2010). The role of water in generating the calc-alkaline trend: new volatile data for Aleutian magmas and a new tholetiitic index. *Journal of Petrology* **51**, 2411–2444.